

# ACTA PHYSICA DEBRECINA

TOM. XLIII.  
2009.

ADIUVANTIBUS

DEZSŐ BEKE, ISTVÁN LOVAS, ÁGNES NAGY,  
JÓZSEF PÁLINKÁS, KORNÉL SAILER  
ET ILONA TAMÁSSY–LENTEI

REDIGIT  
ZOLTÁN TRÓCSÁNYI

REDACTOR TECHNICUS  
*SÁNDOR NAGY*

4010 DEBRECEN, HUNGARIA  
DEBRECEN, 2009.

The coloured electronic version of the articles can be downloaded from our  
homepage: <http://acta.phys.unideb.hu/>.

### **Acknowledgement**

This issue of the **ACTA PHYSICA DEBRECINA**,  
was supported by the *Hungarian Academy of Sciences*.  
This support is highly appreciated and gratefully acknowledged.

Készült a Debreceni Egyetem Egyetemi és Nemzeti Könyvtárának  
sokszorosító üzemében  
rotaprint lemezről 200 példányban  
Felelős kiadó: Dr. Fésüs László  
University of Debrecen 2009  
HU ISSN 1789–6088 Acta Physica Debrecina

## CONTENTS

<b>I. Angeli:</b> The kink strength $S$ : a tool for search of structures in experimental $R_Z(N)$ series .....	4
<b>A. Papp, J. Csikai:</b> Lateral flux distribution of thermal and epithermal neutrons around a Pu-Be source .....	10
<b>V. Takats, M. Trunov, A. Csik, I. Csarnovics, Cs. Cserháti, S. Kokenyesi:</b> Direct fabrication of surface reliefs in amorphous chalcogenide layers .....	15
<b>F. R. Soha, I. A. Szabó, L. Harasztosi, J. Pálunkás, Z. Csernátony:</b> Development of an accelerometer based motion analisys system for biomedical applications .....	23
<b>I. Tamássy-Lentei:</b> Ab initio gas-phase cation affinity study of alkaline for selected alkali, mixed alkali and hydrogenated alkali complexes .	31
<b>Zs. Gulácsi:</b> Delocalization effects treated exactly in strongly correlated systems .....	33
<b>Á. Nagy:</b> Entropic uncertainty relations .....	37
<b>S. Nagy, I Nándori, K. Sailer:</b> Topological phase transition as a crossover .....	44
<b>G. J. Halász, A. Papp, C. Woywod, Á. Vibók:</b> Investigation of higher lying excited states of pyrazine .....	51

## THE KINK STRENGTH $S$ : A TOOL FOR SEARCH OF STRUCTURES IN EXPERIMENTAL $R_Z(N)$ SERIES

I. Angeli

Institute of Experimental Physics, University of Debrecen. H-4010 Debrecen,  
Pf. 105. Hungary

### Abstract

It is shown that the kink strength  $S$  - based on the second difference in nuclear charge radii along isotopic series  $R_Z(N)$  - renders it possible to discover slight changes in the slope. These slope changes, often covered by odd-even effects and statistical scattering of the individual points, are hardly perceptible for the eye. Based on the kink strength  $S$ , a quantitative criterion is introduced, which helps to distinguish real structures from statistical fluctuations.

### I. Introduction

Changes in nuclear structure, as shell effects or deformation, give rise to changes in the mass number dependence of nuclear charge radii  $R = \langle r^2 \rangle^{1/2}$ . Along isotopic sequences, these small variations, "kinks" in the slope of  $R_Z(N)$  series cannot be easily discerned, especially if they are blurred by even-odd staggering. This is illustrated in Figure 1 for an hypothetical isotopic series: the smooth component of the  $R_Z(N)$  curve consists of four linear sections with two positive and one negative kinks between them at neutron numbers  $N = 74, 82$  and  $90$ . These small slope changes are at about the limit of visual observability. Superimposing the even-odd effect, makes these slope changes practically imperceptible in the upper combined curve  $R_Z(N)$ . One way of solving this difficulty is the investigation of *second*

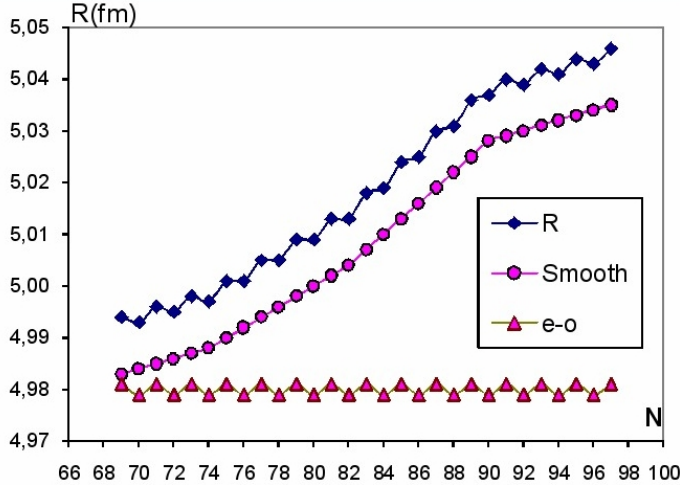


Figure 1: The *smooth* and *even-odd* components of an hypothetical  $R_Z(N)$  isotopic series. For better visibility, the smooth curve is shifted down by 0.01 fm, while the even-odd staggering ( $\pm 1$  am) curve is shifted up by 4.98 fm.

*differences*, which is well known in calculus (introduced by Thomas *Simpson* in the XVIIIth century), and have been applied sometimes in physics, too, e.g. in searching for weak peaks over an intensive background in gamma-ray spectrometry [1].

The effect of the even-odd staggering can be eliminated by the use of  $dN = 2$  intervals in calculating the radius differences  $dR$ . The cost of this advantage is the increase of the peak width in the second difference to  $dN = 2$ , and the loss of the first and last two points. However, as one can see in Figure 2, the gain is well worth the cost: a peak shows not only the position of the respective kink but its amplitude yields a *quantitative measure* of the slope change as well.

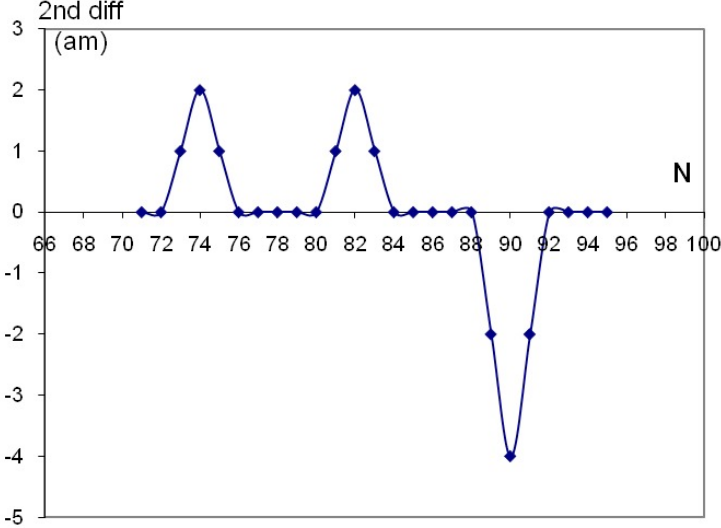


Figure 2: The second difference of the  $R_Z(N)$  data series of Figure 1, using neutron number intervals  $dN = 2$ .

## II. The “kink strength” $S$ , and its application to nuclear charge radii

A nucleon added to a heavy nucleus produces smaller radius increase  $dR$  than that added to a light one, as it is distributed on a larger surface. This trivial mass number dependence can be compensated by multiplying the radius difference with  $A^{2/3}$ . Therefore, the slope change will be characterized by the *kink strength* defined as:

$$S_Z(N) = \frac{d^2 R_Z(N)}{d(2N)^2} \times A^{2/3} \quad (1)$$

For simplicity, in what follows, the short form  $S$  will be used, wherever the subscript and argument are not necessary. As an example, the well-known magic neutron number  $N_M = 50$  has a kink strength  $S = 0.75(1)$  fm in the isotopic series of  $Kr$ , while  $0.95(1)$  fm in  $Rb$ ,  $Sr$  and  $Zr$  alike.

Figure 3 shows the neutron number dependence of two actual isotopic series:  $In$  and  $Cs$ , while on figure 4 the kink strength  $S$  is plotted for

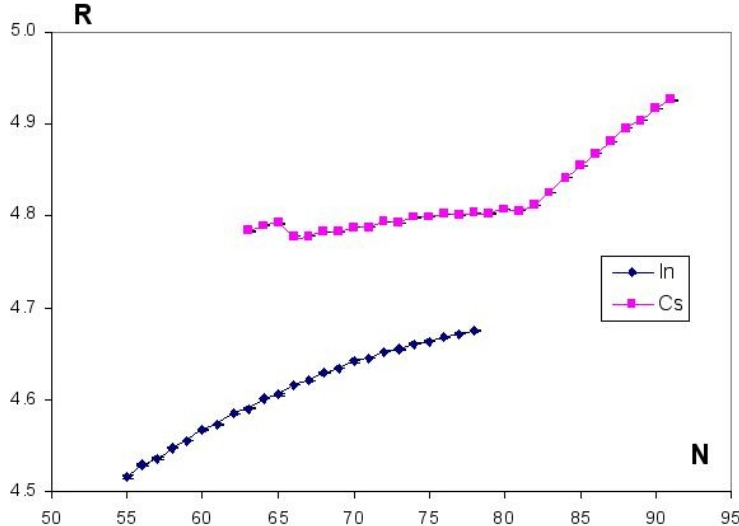


Figure 3: Actual *rms* charge radius data for indium and cesium. Radius data are from [2, 3, 4]; see also [5, 6, 7, 8].

the same elements; original *rms* charge radius data are from [2, 3 and 4], see also [5, 6, 7, 8]. In order to prevent confusing the points of the two different series, the curve for *Cs* is shifted up by one unit in  $S$ , see also the identification symbols. One can see that the data series for *In* follows practically a smooth, constant line, while for *Cs* there are several significant structures. One of these, at the neutron number 82, is readily interpreted as the shell closure and opening a new shell at the magic number  $N = 82$ , while the others - both positive and negative - arise probably from deformation changes around the encounter of the very different  $3s_{1/2}$  and  $1h_{11/2}$  levels. However, this conjecture should be checked by detailed theoretical calculations.

More curves and tables of *significant* numerical  $S$  values for isotopic - and also for isotonic - curves have been published elsewhere, see tables A1 and A2, as well as figure A1 in the Appendix of [9]. Here *significance* means that the absolute value of  $S$  should be higher than 0.2 and also higher than three times its error, i.e. an  $S$  value is regarded significant if

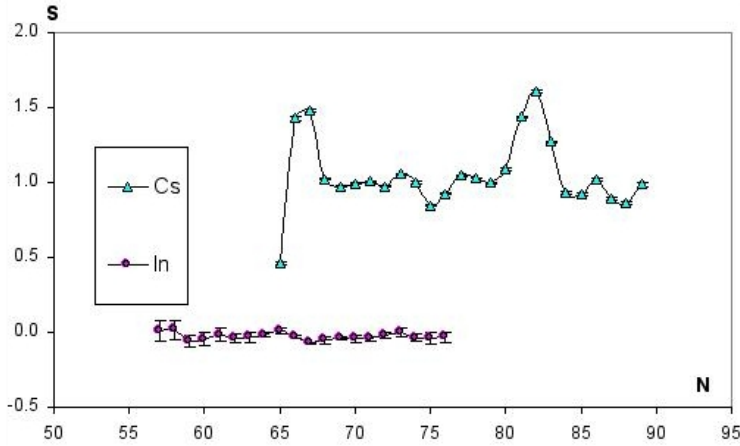


Figure 4:  $S_Z(N)$  kink strength values derived from actual *rms* charge radius data of the isotopic series of indium and cesium. Data for *Cs* are shifted up by one unit in  $S$ .

$|S| > 0.2$ , and  $|S| > 3 \times \Delta S$ . It is hoped that these rather rigorous criteria prevent noticing false structures. New kinks discovered in this way, may be compared to the behaviour of other nuclear characteristic quantities for the region in question, as quadrupole moments or deformation parameters, as well as the energy of the first excited states. These empirical data taken together, may yield further food for theoretical studies of nuclear structure.

## References

- [1] P. Raics: Personal Communication.
- [2] A. Coc, et al.: Nucl. Phys., **A468** (1987) 1.
- [3] J. Eberz, et al.: Nucl. Phys., **A464** (1987) 9.
- [4] C. Thibault, et al.: Nucl. Phys., **A367** (1981) 1.

- [5] I. Angeli, Recommended values of nuclear charge radii - 2008. In:  
<http://cdfe.sinp.msu.ru/services/radchart/radmain.html>
- [6] G. Fricke, K. Heilig, Landolt-Börnstein: Num. Data and Funct. in Science and Tech. New Series, Group I: Elem. Part., Nuclei and Atoms, v. **20** (2004).
- [7] Yu. Gangrsky, and K.Marinova, Nuclear charge radii - 2008. In:  
<http://cdfe.sinp.msu.ru/services/radchart/radmain.html>
- [8] E.W. Otten, in: Treatise on Heavy-Ion Science, Vol. **8**, ed. D.A.Bromley (Plenum Press, New York, 1989) p. 517.
- [9] I. Angeli, et al.: Journ. Phys. G: Part. Nucl. Phys., **36** (2009) 085102.

**LATERAL FLUX DISTRIBUTIONS OF THERMAL AND EPITHERMAL NEUTRONS AROUND A Pu-Be SOURCE****A. Papp<sup>1</sup>, J. Csikai<sup>1,2</sup>**<sup>1</sup> Institute of Nuclear Research of the Hungarian Academy of Sciences, 4001 Debrecen, Pf. 51, Hungary<sup>2</sup> Institute of Experimental Physics, University of Debrecen, 4010 Debrecen-10, Pf. 105, Hungary**Abstract**

Lateral flux distributions of neutrons produced by a Pu-Be source in the interface of moderator and reflector have been measured by a twin  $BF_3$  counter. The FWHM values of flux distributions measured along, perpendicular and diagonal directions to the longitudinal axis of the counters were found to be 20cm, 21cm and 15cm, respectively. The relative excess counts,  $(I - I_0)/I_0$ , as a function of the distance from the center exhibit maxima with values of 0.46 and 0.13 with and without a  $Cd$  layer, respectively. Background ( $I_0$ ) measured with sand moderator without  $Cd$  layer is  $\sim 14$  times higher than that obtained with cadmium. Results render the determination of the volume of the interrogated region for bulk hydrogen analysis and the spatial resolution of the hand-held neutron detectors used for the observation of plastic anti-personnel landmines possible.

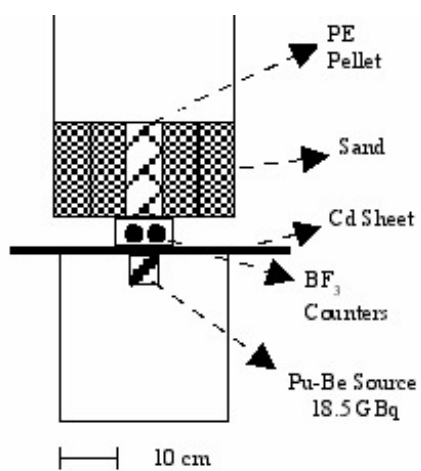
**I. Introduction**

Various neutron based techniques used for bulk hydrogen analysis and the detection of anti-personnel landmines (APMs) have been developed under the Co-ordinated Research Programs (CRPs) of the IAEA starting in

1997 and 1999, respectively, [1], [2]. Some results achieved in this international collaboration were described in a Special Issue of ARI in 2004 [3] and in a recent survey on the status of humanitarian demining [4]. Most of these methods require the knowledge of the flux distributions of thermal and thermalized epithermal neutrons measured in the interface between the moderator and the reflector, in addition to the dependence of neutron yields on the depth of the object and on the stand-off distance of the detector [5]. These data are important especially for the improvement of the hand-held neutron thermalization detectors as well as for the identification of contrabands in airline baggages and cargo containers containing plastic explosives. The present investigations were undertaken with the aim to complete our previous studies [6] on the flux distributions of neutrons in the interface of the moderator and the reflector measured by the prompt detection of neutrons instead of the foil activation method.

## II. Experimental

In the present experiments neutrons were produced by a  $Pu - Be$  source of 18.5 GBq, ( $5.25 \cdot 10^6$  n/s intensity) placed along the central line of a cylindrical hydrogenous moderator of 30 cm in diameter, made of  $\epsilon$ -caprolactam ( $C_6H_{11}ON$ ). The active volume of the source was about 2 cm under the surface. A  $Cd$  sheet put on the surface of the moderator has been used to produce a plane source of epithermal neutrons with a dimension of about 33cm  $\times$  33cm. Yields of thermal and thermalized epithermal neutrons were detected by two  $BF_3$  counters of 14cm length and 2.3cm diameter sensitive dimensions connected in parallel. The experimental arrangement of this so-called Epithermal Neutron Analyzer (ETNA) [7] is shown in Fig.1. Dry sand poured in beer-cans has been used as reflector and we replaced them in different positions one by one with a can containing granulated polyethylene (PE) in order to measure the flux distributions both for thermal and thermalized epithermal neutrons. The photo (B) in Fig.1 demonstrates the matrix of cans filled with sand and granulated PE. The lateral flux distributions of thermal and epithermal neutrons were measured also on the surface of the moderator without reflector by moving the  $BF_3$  detectors in left and right directions.



(a)



(b)

Figure 5: Schematic diagram of the ETNA measuring arrangement (a) and a photo on the matrix of the sand and polyethylene reflector (b).

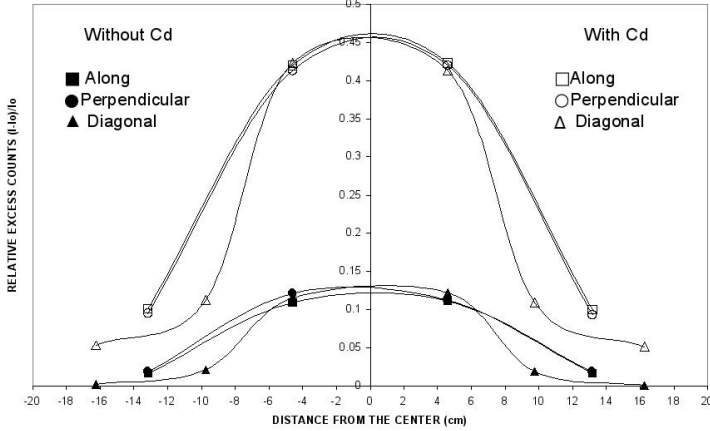


Figure 6: Lateral flux distributions of neutrons measured with and without Cd layer.

### III. Results and discussion

The lateral flux distributions of thermal and epithermal neutrons measured along, perpendicular and diagonal directions to the longitudinal axis of the counters with and without a *Cd* layer can be approximated by a second order polynomial. As shown in Fig. 2 the relative excess counts,  $(I - I_0)/I_0$ , as a function of the distance from the geometrical center exhibit maxima at 0.46 and 0.13 with and without a *Cd* layer, respectively. Background ( $I_0$ ) measured in the interface with a sand moderator of saturation thickness without *Cd* layer is  $\sim 14$  times higher than that obtained with cadmium. A value  $\sim 12$  obtained for the ratio of the backgrounds on the surface of the moderator without reflector indicates the sky-shine effect of thermal neutrons.

The FWHM values deduced from the lateral flux measurements on the free surface of moderator with and without *Cd* were found the same  $\sim 13$  cm. However, the 20cm, 21cm and 15cm FWHM values obtained for the flux distributions with reflector and *Cd* clearly indicate the advantage of using

epithermal neutrons for the detection of plastic landmines and identification of contrabands.

### Acknowledgement

This work was supported in part by the Hungarian Academy of Sciences.

### References

- [1] IAEA, *Bulk Hydrogen Analysis Using Neutrons*, (IAEA/PS/RCM/97-1, Vienna, Austria, 1997).
- [2] IAEA, *Application of Nuclear Techniques to Anti-Personnel Landmines Identifications*, (IAEA/PS/RC-799, Vienna, Austria, 1999).
- [3] Applications of Nuclear Techniques to Anti-personnel Landmine Identification, Applied Radiation and Isotopes, Special Issue, (Eds: J. Csikai, E. Hussein, U. Rosengard) **61**, 1 (2004).
- [4] R. Dóczki, Acta Physica Debrecina **XLI**, 41 (2007).
- [5] J. Csikai, B. Király, R. Dóczki, Application of Neutrons to Plastic Landmines Detection, in Proc. of *2<sup>nd</sup> RCM on Nuclear Demining Techniques*, (IAEA/PS/RC-799-2) St. Petersburg (2001).
- [6] B. Király, J. Csikai, Appl. Radiat. Isot. **52**, 93 (2000).
- [7] J. Csikai, R. Dóczki, Appl. Radiat. Isot. **67**, 70 (2009).

**DIRECT FABRICATION OF SURFACE RELIEFS IN  
AMORPHOUS CHALCOGENIDE LAYERS**

V. Takats<sup>1</sup>, M. Trunov<sup>2</sup>, A. Csik<sup>1</sup>, I. Csarnovics<sup>3</sup>, Cs. Cserháti<sup>3</sup>, S. Kokenyesi<sup>3</sup>

<sup>1</sup> ATOMKI, Debrecen, Hungary

<sup>2</sup> Uzhgorod National University, Uzhgorod, Ukraine

<sup>3</sup> University of Debrecen, Debrecen, Hungary

**Abstract**

Processes of one-step surface relief (ridges and grooves) formation on  $As_xSe_{1-x}$  ( $0 \leq x \leq 0.5$ ) and  $As_2S_3$  layers, as well as on  $Se/As_2S_3$  nanomultilayers, stimulated by laser illumination or e-beam, were investigated. Permanent changes of the spontaneous relief have been observed under uniform illumination and the profile formation during holographic or direct e-beam recording in the same materials was analyzed. Mechanisms of the above processes are related to the peculiarities of stimulated structural transformation as well as to the changes of optical parameters and induced mass-transport. Chalcogenide compositions and nanostructures with best volume expansion were selected. It was shown that optical elements can be fabricated in such one-step direct recording processes.

**I. Introduction**

Chalcogenide glasses like  $As_2S_3$ ,  $AsSe$ ,  $GeSe_2$  and similar compounds, amorphous layers on their basis reveal photo-induced structural transformation effects within amorphous phase and related changes of optical parameters [1,2] as well as of chemical stability [3]. Thus these materials offer

applications of these materials as high-resolution inorganic photo-resist, for example for diffraction grating fabrication [3]. In spite of some shortcomings of such “wet technology” diffraction gratings and other optical elements (flat lenses, lens arrays, waveguides with high performance in VIS and especially in IR spectral range) can be fabricated this way.

Furthermore very peculiar effects like photo-plasticity or photo-fluidity [4,5], stimulated expansion or contraction [6,7] also appear when chalcogenide layers are illuminated, or irradiated by e-beam. However, up to now these are rather ambiguously correlated with composition and experimental conditions. What is more, giant expansion was also observed due to the photo-stimulated interdiffusion in chalcogenide nano-multilayers [8]. All these data show the prospects of direct, one-step recording process, without any post-treatment, which may be especially useful for prototyping photonic elements. Glasses from  $As_xSe_{1-x}$  system ( $0 \leq x \leq 0.5$ ) with well known model structure and rather easy technology, reveal almost all of the above-mentioned effects. They are sensitive in the red spectral region, where their optical absorption edge  $E_g^o$  is located. In our present paper particular emphasis is given to recording of surface gratings with sinusoidal profile on the selected film compositions and nanomultilayers and to the comparison of these data with separate line formation process under the influence of focused e-beam.

## II. Experimental

Raw glasses were prepared by the conventional technology of synthesis in evacuated quartz ampoules from high purity *As*, *S* and *Se* materials. Homogeneous films with total thickness *d* between 0.7-1.8  $\mu m$  were fabricated by physical vapor deposition on silica glass substrates. To obtain layered, nano-modulated film structures, bulk  $As_2S_3$  and *Se* were evaporated from isolated Tantalum boats onto polished silicon or microscope slide glass substrates by computer guided cyclic thermal evaporation method. The modulation periods were usually equal to  $\Lambda = 6$  nm with  $d(As_2S_3) = 3$  nm and  $d(Se) = 3$  nm in sub-layers. The total number of bi-layers was 100-200. The quality and period of samples were controlled by low angle x-ray diffraction method (LAXRD). Film thickness was measured in direct way by Ambios XP-1 nanoprofilometer. Optical transmission spectra were measured by

Shimadzu -3600 spectrophotometer, simple changes of transmission - by a photodiode. All experiments except of e-beam recording were made in a normal atmosphere conditions, at room temperature.

Optical recording of surface structures (geometrical, lateral and vertical, and at the same time optical amplitude-phase relief of changes of optical transmission and refraction) was performed on a laboratory holographic kit. It enables us to create periodical (close to the sinusoidal) distribution of the coherent light intensity in the spot of approximately 3 mm in diameter on the investigated chalcogenide layer. The recording was performed at  $\lambda = 0.63\mu\text{m}$  and  $\lambda = 0.53\mu\text{m}$ , with average power densities near  $0.8 \text{ W.cm}^{-2}$ . Periodical relief formation was followed by readout of the diffraction efficiency in the reflecting mode ( $\lambda = 0.44\mu\text{m}$ , well above the optical absorption edge  $E_g^0$  for the given compositions of semiconductor glasses), as well as in the transmission mode ( $\lambda = 0.65\mu\text{m}$ , near or below the appropriate  $E_g^0$ ). Data were compared with direct surface relief measurements which were performed by SPM. Scanning was made in non-contact mode.

Light induced surface transformation was compared with the development of lines (ridges) during e-beam irradiation in the Hitachi S-4300 scanning electron microscope. The accelerating voltages were changed between 10 -25 kV, currents near 10 nA, but the cycle of time-dependent relief development was done at 15 kV. Samples were covered with 50 nm gold layer to avoid surface charging, but some experiments were made on a clean surface too.

### III. Results and discussion

It was established that pure, micrometer-thick  $As_xSe_{1-x}$  ( $0 \leq x \leq 0.5$ ) as well as  $As_2S_3$  layers possess photo-darkening under laser illumination. It was weak (few percent of initial transmission  $\tau_0$  at  $\lambda = 0.65\mu\text{m}$ ) in  $As_xSe_{1-x}$  layers with  $0 \leq x \leq 0.3$ , illuminated with red laser beam, as well as in  $As_2S_3$  under green laser illumination. The  $Se/As_2S_3$  nanomultilayers (NML) are sensitive both to the red and green light and reveal photo-bleaching, as it is shown in Figure 1. First of all the Se-containing NML's were analyzed and compared with the above mentioned single layers. The best recording conditions can be determined from the changes of optical transmission spectra, due to the illumination ( $\Delta\tau$  and  $\Delta n$ ), as well as from the height of the surface geometrical relief ( $\Delta d$ ).

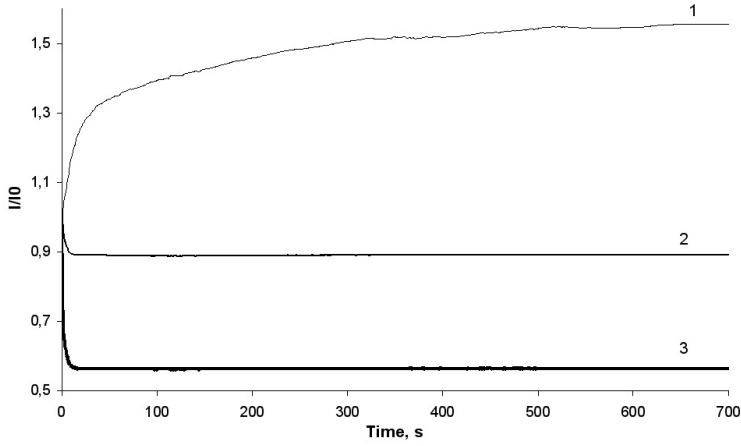


Figure 7: Change of optical transmittance relative to the initial one under red laser irradiation in  $Se/As_2S_3$  NML (1),  $As_{0.2}Se_{0.8}$  layer (2) and in  $As_2S_3$  layer under green laser illumination (3).

In spite of the relatively small changes of optical transmittance (darkening due to the stimulated changes of structural disorder [1,2] in the selected compositions or bleaching due to the stimulated interdiffusion in NML [8]) they all exhibit giant (up to 10-15 % of the total thickness) surface deformations in illuminated spots. These can be used for phase modulation of the reflected or transmitted light. It was established that in the single layers the “spontaneous” formation of quasi-periodical surface ridges and grooves in small, random spots takes place under illumination (see Figure 2.). Really periodical structures were developed in homogeneous layers and in NML under holographic recording, i.e. under periodical distribution of excitation according to the lateral interference pattern.

According to the results on similar effect in Ag-containing photosensitive layers [9], the mechanism of the observed “spontaneous” surface roughening, at the first stage, can be connected with formation of local interference patterns due to the inhomogeneity of thin film thickness, i.e. creation of lateral distribution of absorbed photons. The further absorption is a self-enhanced process, creating build-in gradients of excited bonds, defects and non-equilibrium carriers and, in the presence of essential “athermal softening”

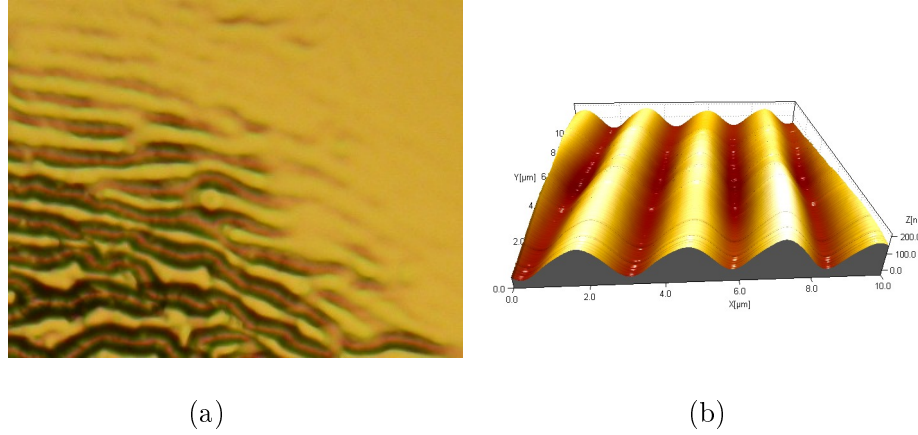


Figure 8: a) Spontaneous surface reliefs on the surface of illuminated  $As_{0.2}Se_{0.8}$  layer (optical microscope image). b) AFM picture of the surface holographic grating in the same layer.

ing” of the illuminated chalcogenide glass (due to the photo-plastic effect [4]) causing lateral mass transport from the dark to the illuminated strips. The real mechanism of such lateral mass-transport is not completely clear yet. The vertical mass-transport due to the interdiffusion in NML can be explained by the same “softening” of adjacent sub-layers and creation of solid solutions with optical parameters and density, which differ from the components. It should be mentioned that evidently in both types of sensitive layers the native volume changes near 1% under structural transformations exist [10], but they are only the smallest component of the total deformation.

If the above described mechanism is true, similar recording can be produced in investigated samples by e-beam, which can create localized excitation in the layer. We have realized this type of direct e-beam recording on single  $As_xSe_{1-x}$  and  $As_2S_3$  layers, as well as on  $Se/As_2S_3$  NML structures (see Figure 3.).

Further comparison of important recording parameters, i.e. the change of the optical transmission, refractive index and thickness in a number of compositions, made possible the conclusion that  $As_xSe_{1-x}$  ( $0 \leq x \leq 0.3$ )

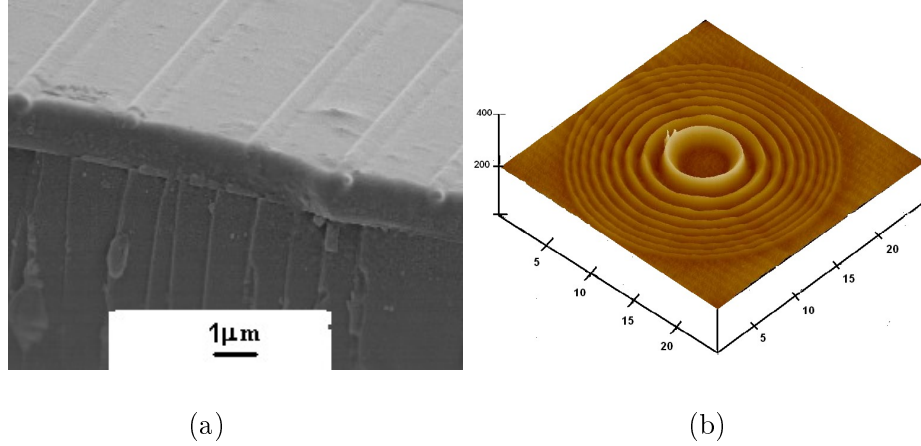


Figure 9: a) SEM picture of e-beam recorded lines on  $As_2S_3$  layer (cross-section of the layer on glass substrate), b) AFM picture of e-beam recorded Fresnel-lens on  $Se/As_2S_3$ .

and  $As_2S_3$ , as well as  $Se/As_2S_3$  NML are applicable for efficient direct surface relief fabrication. Small addition of  $As$  to  $Se$  is desirable for better temperature stability of the material and larger photo-plastic effects [11]. In  $Se/As_2S_3$  NML the stimulated expansion obviously occurs in irradiated  $Se$  and  $As_2S_3$  sub-layers before and during the interdiffusion, as well as after it in the mixed  $As - S - Se$  layer. Thus at least three components have contributions and, together with known effect of photo-induced viscosity change, result in high surface deformations. This assumption was supported by separate investigations of surface relief formation during holographic recording of periodical structure (grating) and simple line (ridge) formation by scanning focused e-beam on the surface.

#### IV. Summary

Direct, one-step process of surface relief formation on  $As_xSe_{1-x}$  ( $0 \leq x \leq 0.5$ ) and  $As_2S_3$  layers, as well as on  $Se/As_2S_3$  nano-multilayers can be realized by laser or e-beam recording. Spontaneous relief formation under illumination as well as the given profile fabrication are connected with non-

uniform localized excitation in presence of enhanced photo-plastic effect in these materials. It is shown that optical elements can be fabricated in such one-step direct recording processes.

### Acknowledgements

This work was supported by bi-lateral R&D Grant UA 17/2008 as well as by NKTH-OTKA Grant K67685.

### References

- [1] M. Popescu, *Non-Crystalline Chalcogenides*, (Solid State Science Technology Library, **8**, Kluwer Academic Publishers , 2000).
- [2] A. Kolobov, K. Tanaka (in *Handbook of Advanced and Photonic materials and Devices*, Ed. H.S. Nalva, Acad.Press, 2001).
- [3] E. Venger, A. Melnichuk, A. Stronskyi, (*Photo-stimulated processes in vitreous chalcogenide semiconductors and their applications*, Ed.h. Academperiodica, Kijev, 2007). (in Russian).
- [4] K.Tanaka, Phys.Rev. B**57**, 5163(1998).
- [5] S.N. Yannopoulos, M.L. Trunov, Phys. Status Solidi B**246**, 1773 (2009).
- [6] G. Chen, H. Jain, M. Vlcek, A. Ganjoo, Phys. Rev. B**74**, 174203 (2006).
- [7] G.B. Hoffman, W.C. Liu, W. Zhou, R. Sooryakumar, J.Vac.Sci.Technol. B**26**, 2478 (2008).
- [8] S. Kokenyesi, Journal of Optoelectronics and Advanced Materials, **8**, 2093 (2006).
- [9] L.A. Ageev, V.K. Miloslavsky, V.V. Bloha, N. Assad, Surface. Physics, chemistry, mechanics, **12**, 31(1987). (in Russian).

- [10] D.M. Bercha, A.A. Kikineshi, M.I. Marjan, Ukr. Phys. Journal, **26**, 978 (1981). (in Russian).
- [11] M. L. Trunov, P. M. Nagy, V. Takats, P.M. Lytvyn, S. Kokenyesi, E. Kalman, J. Non-Crystalline Solids, **355**, 1993 (2009).

**DEVELOPMENT OF AN ACCELEROMETER BASED  
MOTION ANALYSIS SYSTEM FOR BIOMEDICAL  
APPLICATIONS****F. R. Soha<sup>1</sup>, I. A. Szabó<sup>1</sup>, L. Harasztosi<sup>1</sup>, J. Pálinkás<sup>2</sup>, Z. Csernátony<sup>3</sup>**<sup>1</sup> University of Debrecen, Department of Solid State Physics<sup>2</sup> University of Debrecen, Department of Physiotherapy<sup>3</sup> University of Debrecen, Orthopedic Clinics**Abstract**

The kinematics of motion contains a lot of information on the biomechanics and the internal state of the subject. Kinematics data must be collected under the most natural conditions and properly processed to provide information of diagnostic value.

We describe an inertial sensor based motion analysis system, which was developed in our laboratory. Details of the measurement system, the calibration and the validation procedure are presented.

A data evaluation procedure is described for the analysis of quasi-periodic motions. Finally, results of gait signal analysis are shown to demonstrate the applicability of the system for biomedical studies.

**I. Introduction**

The experimental study of the kinematics of biomechanical systems provides important data for research and applications. The registered signals during the motion show individual differences and variations. These differences represent the difference in the biomechanics of the subjects, and also the changes in internal state and the influence of external disturbances. The

separation of these factors requires the collection and analysis of large sets of data and the development of proper data processing technologies. The individual characteristics of a given type of motion can be exploited for identification or diagnostic purposes. Changes of the individual characteristics can be used to monitor internal changes in the subject's physiological or mental state. The efficiency of a treatment in rehabilitation or sport training can be followed through the comparison of measurements of the same motion performed at different times [1].

The main requirement for the measurement is that it should have a minimal influence on the subject. This includes the direct effect of the motion detection system on the subject and also the situation in which the motion analysis is performed. There is a long tradition of motion analysis in laboratory settings with commercial equipments. The small range of possible motions, the unnatural settings, and the cost both in time and money are inhibiting its application for larger scale studies. Using the recent developments in sensor technology and microelectronics one can develop inexpensive motion analysis systems, which can be applied outside the laboratory [2].

In this article, we describe an inertial sensor based data collection and analysis system and its application for gait analysis.

## II. Experimental setup

The measurement system consists of a data logger modul and three sensor moduls. The data logger is based on an Atmel ATMEGA-128 microcontroller. The analog signals are periodically sampled using the internal AD converter of the microprocessor. The collected data is written on an MMC card interfaced to the microcontroller.

The data logger has a one button interface, which can be used to start and stop the measurement. Acoustic feedback is provided by a buzzer to the user about the normal operation or internal error (like a missing MMC card). Two LEDs shows the state of operation (powered on, standby, measuring). Data is transferred to the pc using the MMC card. Files of the different measurements are sequentially numbered by the logger and can be directly read by the data evaluation software on the PC.

The sensor units are connected through USB type connectors to the data

logger. These connectors provide firm contact during normal use, but can easily be disjoined, which is important for safety and convenience reasons. The data logger unit provides the power to the sensor units and receives the analog sensor outputs for the three acceleration channels.

We have chosen the MMA 7620Q accelerometer sensors (Freescale Inc., USA, Austin). The acceleration sensitivity can be set to four different levels. Two ranges are applicable for small accelerations up to 1.5g and 2g and two ranges are applicable for higher accelerations up to 4g and 6g limits. The limit is set by jumpers on the individual sensors before the measurement.

The accelerometer data presents the dynamic accelerations and to the static acceleration of the earth's gravity together. The static acceleration can be used for direct calibration of the sensors.

Accelerometer sensor calibration is performed relative to the earth's gravity. The sensor box has a brick shape. The sensor box is placed on a flat horizontal surface six times with different sides facing upwards. (see Figure 1.). The voltage reading for each axis corresponds to the 1g, -1g or 0g value for each configuration. Voltage data is averaged for the time intervals corresponding to a given configuration. The calibration software calculates the conversion factors between the voltage and the acceleration for each axis. The calibration can be easily performed before the actual measurement. In this way systematic errors related to the drift of sensitivity and zero point with temperature can be eliminated.

The measurement setup can include a video camera for recording the motion. The video recording provides documentation for the measurement. The subject of the measurement can receive various instructions or the performed motion can change for other reasons. These events are recorded on the video, and can be used to later to segment the acceleration measurement into different parts.

### III. Data analysis

The analysis is performed off line on the data files transferred to a PC. The main steps of the processing are the data conversion, signal synchronization, segmentation and analysis. The software was written in LabVIEW because it provides a large number of signal analysis functions and an easy way to develop user interfaces.

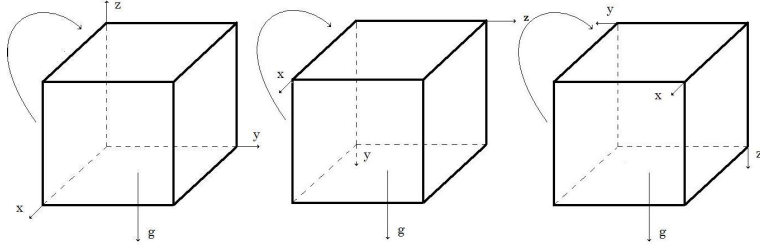


Figure 10: Sequence of sensor positions for the z axis calibration.

The first step of the data processing is the data conversion. The measured sensor signal voltages are converted to acceleration data. This step is performed based on the evaluation of the sensor calibration results performed before the measurement. The recoded video signals also have to be converted to proper format for viewing on the pc. This conversion was performed with separate programs. The original interlaced video was converted to a double frame format, providing a slow motion recording with half speed.

The second step is the synchronization of the video stream with the acceleration data. For synchronization, the most easily recognizable sensor signal is used. For example for walking the heel strike position gives the largest acceleration data for a sensor attached to the knee. This moment can easily recognized on video as well. After the adjustment of the starting positions, the image and the accelerometer data remains in sync for the whole measurement. This can be easily checked with the comparison of later heel strikes.

The third step is the selection of data segments based on the recorded video data by the user. This step and the synchronization is performed with a program, which can show both the vide frames and the acceleration data for any sensor axis. The user can give name to data segments, and identify start and end points based on the recorded data. These segments are individually analyzed in the subsequent data processing steps, which are specific to the biomedical application.

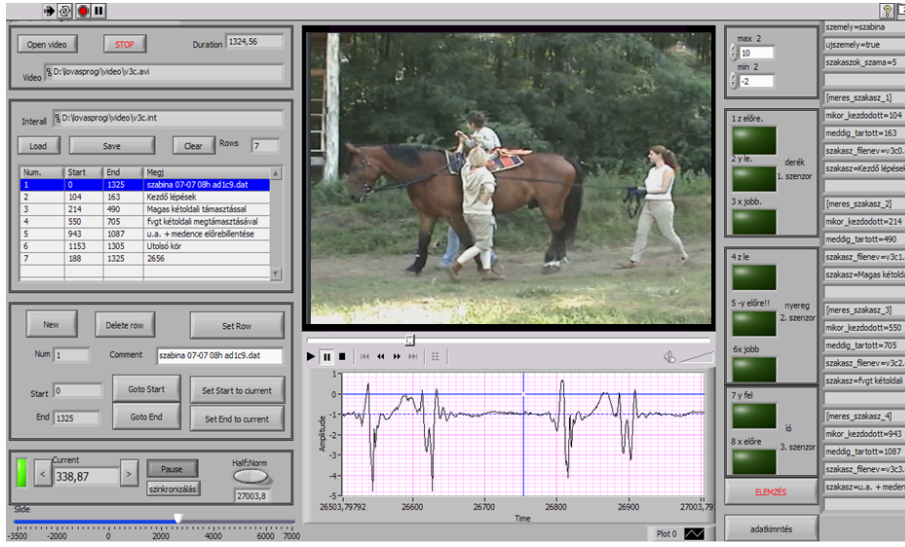


Figure 11: Video and acceleration data synchronization and segmentation.

#### IV. System validation

We have tested the measuring system with known motion of a simple oscillator. A vertically arranged mass and spring system was constructed. The mass was a long iron bar, which was excited with an external coil close to the resonance frequency. The range of motion and the acceleration values were selected to be in the range of the hippotherapy measurements. For the measurements, both the data collection unit and the sensors, or only the sensors were attached to the moving bar. This corresponds to the measurement setup during motion analysis. The amplitude of the steady state vibration was measured optically with a telescopic system. The collected data was filtered for the sensor noise, and the resulting signal was processed with a single tone analysis routine to extract the amplitude of the acceleration. In this way, we have validated the whole measurement setup and data evaluation procedure.

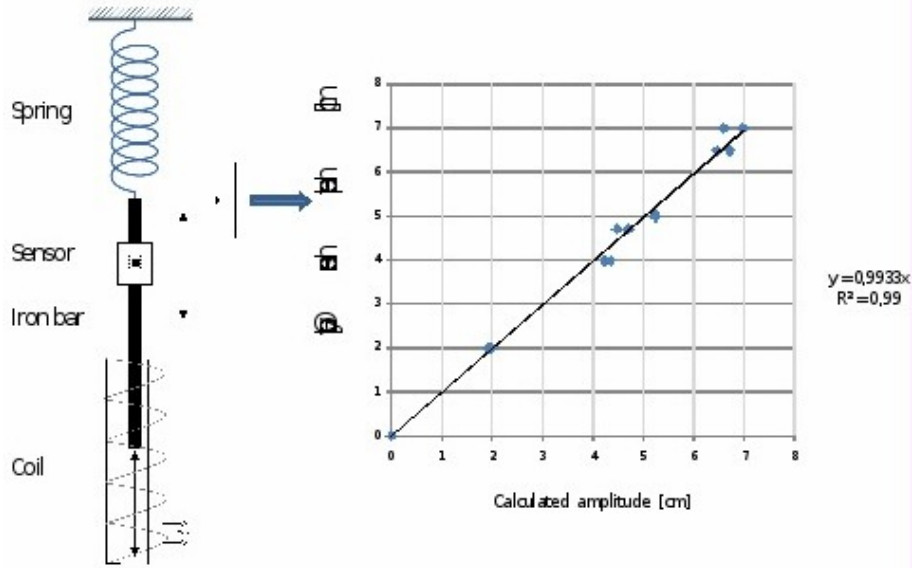


Figure 12: Setup and calibration data for system validation.

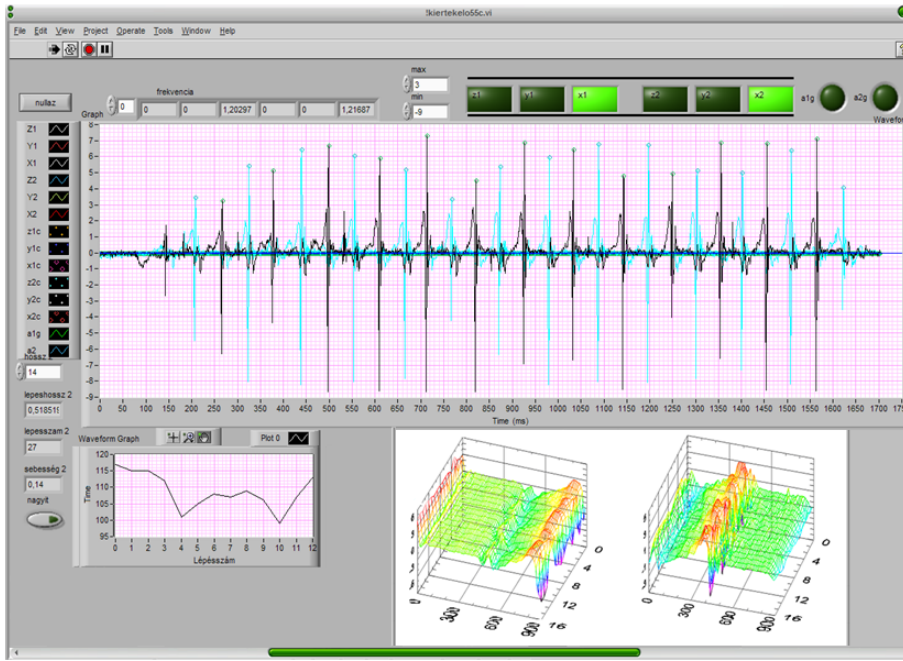


Figure 13: Acceleration data analysis for gait study.

## V. Application to gait analysis

The sensors are attached to the knee's on the two legs for gait analysis. This provides a large signal for heel strike, which is used to decompose the signal to gait periods.

One of the evaluation procedures is the averaging of quasi periodic motion sequences. The periods are identified by a peak acceleration values. Time variation is taken into account by scaling the signals to the average period in the temporal direction. Then the accelerations are averaged for a large number of steps at different phases. In this way the small step by step variations and the sensor noise can be averaged out.

## References

- [1] Richard Baker, Gait analysis methods in rehabilitation J. of Neuro-Engineering and Rehabilitation **3**, 4 (2006), doi:10.1186/1743-0003-3-4.
- [2] Kavanagh JJ, Menz HB., Accelerometry: a technique for quantifying movement patterns during walking. Gait Posture **28**(1), 1–15 (2008).
- [3] Tom Chau, Scott Young and Sue Redekop, Managing variability in the summary and comparison of gait data J Neuroengineering and Rehabilitation **2**, 22 (2005), doi: 10.1186/1743-0003-2-22
- [4] Pálinkás, J., Szabó, I., Harasztosi, L., Vass, Sz., Soha, F., & Csernátony, Z., Comparison of different equilibrium examining methods, A pilot study: examination of the improvement in balance after hippotherapy. Biomechanica Hungarica **2**(1), 51–58 (2009).

**AB INITIO GAS-PHASE CATION AFFINITY STUDY OF  
ALKALINE FOR SELECTED ALKALI, MIXED ALKALI AND  
HYDROGENATED ALKALI COMPLEXES**

**I. Tamássy-Lentei**

Department of Theoretical Physics, University of Debrecen,  
H-4010 Debrecen, Hungary

Recently the study of the metal cations has gained significant interest especially for the chemists. We studied energies, geometrical structures, stability of such systems [1, 2, 3]. One can also obtain the cation affinity, as a simple difference of the adequate system-energies. The results are important, because very few experimental and theoretical investigations are known concerning these quantities. We used an ab initio approximation applying Gaussian Orbitals. According to this approximation the wave function parameters were treated as variational quantities, using the variational principle of the quantum mechanics. The study was applied to the following systems:  $\text{Li}_n\text{H}_m^+$ ,  $\text{Na}_n\text{H}_m^+$ ,  $\text{Na}_n\text{Li}_m^+$ ,  $(\text{LiH})_n\text{Na}_m^+$ ,  $\text{X}^+(\text{H}_2)_n$  and  $\text{H}^+\text{M}$ ,  $\text{Li}^+\text{M}$ ,  $\text{Na}^+\text{M}$ ,  $\text{K}^+\text{M}$ , where  $\text{M} = \text{LiO}^-$ ,  $\text{LiOH}$ ,  $\text{LiOH}_2^+$ ,  $\text{LiN}^{--}$ ,  $\text{LiNH}^-$ ,  $\text{LiNH}_2$ ,  $\text{LiNH}_3^+$ . The interaction energies obtained for some possible chemical processes are reasonable.

One can also examine the measure of the stability concerning some possible chemical processes. The ab initio calculation shows, that these small cationic complexes are stable in the ground state. We determined the equilibrium geometrical structures and the binding energies of some possible decomposition channels, too. An extension to excited states of the systems discussed are in progress.

## References

- [1] I. Tamássy-Lentei and J. Szaniszló, *Acta Phys. Chim. Debr.* **30/1**, 27 (1995); *ibid* **34–35**, 29 (2002); *ibid* **36**, 57 (2003); *ibid* **37**, 91 (2004).
- [2] I. Tamássy-Lentei and J. Szaniszló, *Acta Phys. Hung.* **51**, 101 (1981); *ibid* **74**, 339 (1994).
- [3] I. Tamássy-Lentei and J. Szaniszló, *J. Mol. Struct. (Theochem)* **501–502**, 403 (2000).

**DELOCALIZATION EFFECTS TREATED EXACTLY IN  
STRONGLY CORRELATED SYSTEMS****Zs. Gulácsi**

Department of Theoretical Physics, University of Debrecen, H-4010 Debrecen,  
Hungary

**Abstract**

Delocalization effects in non-integrable strongly correlated many-body systems holding local Coulomb repulsion are described in exact terms by the use of a positive semidefinite operator technique. An insulator to metal transition is presented in two dimensions together with a transition to a correlated half-metallic state in diamond chains under the action of a perpendicular external magnetic field.

**I. Introduction**

Delocalization effects in low dimensional systems represent nowadays a fascinating subject because seems to contradict established and unanimously accepted rules in the past. In disordered systems for example, despite the scaling theory prohibiting insulator to metal transition in two dimensions, the presence of delocalization effects under the action of the local Coulomb repulsion ( $U$ ) becomes to be an established fact [1].

As opposed to the random case, periodic external potential is also able to cause insulating behavior, hence can be as well used as a starting point in investigating the delocalization effect of  $U$  in non-disordered situations. Such effects have been already observed, for example in the case of the two dimensional ionic Hubbard model [2] attracting considerable attention.

This is motivated by the fact that the ability of  $U$  to drive transitions from conducting to insulating behavior is widely studied and known [3]. But here, unexpectedly, one reaches an interaction driven metallic behavior starting from an insulator, instead to have a transition to an insulating state from a metal, as intuitively is expected.

How is able physically  $U$  to produce a delocalization effect in two dimensions, and what are the other circumstances (if any) in which such effect can also emerge, where subjects intensively investigated by our group. To provide valuable results the study has been done at exact level using a method based on positive semidefinite operator properties [4]. The results are briefly presented in the following Section.

## II. Results

### II.1 Delocalization in two dimensions

One fixed the starting circumstances to those observed during simulations in the case of the ionic Hubbard model [2]. Consequently, one analyzed a two dimensional two-band system at half filling such that in the non-interacting case a band insulator is present as the ground state, which supplementary presents a macroscopic degeneracy. This is achieved by fixing the parameters of the non-interacting part of the Hamiltonian such to have two bare bands separated by a finite gap (lowest band completely filled, upper band empty), the lowest bare band being flat. After this step one turned on the interaction, and analyzed its effect. The possible delocalization has been investigated by calculating the one-particle localization length from the long-range hopping ground state expectation value, the multielectronic ground state being exactly determined [5].

The results show that  $U$  acting on the background of a macroscopic degeneracy present in a multiband type of system, tries to strongly diminish the double occupancy, and for this reason spreads out the contributions in the ground state wave function, hence strongly increases the one-particle localization length. Consequently, in these conditions  $U$  extends the one-particle behavior producing conditions for a delocalization effect. In this

manner, the ground state becomes constructed entirely from extended operators, whose presence is a sign of the strong correlation effects present at half filling in the interacting case, and the one-particle localization length (comparing to the  $U = 0$  case) increases with several orders of magnitude [5]. I further note that in order to construct the resulting extended operators, the system must combine a huge number of linearly independent contributions. If all these contributions are belong to the same energy (e.g. the starting non-interacting case is strongly degenerate), the creation of the interacting ground state is without cost of energy, hence it is easier to be effectuated. This is the reason why macroscopic degeneracy is important for the delocalization process. If the degeneracy is missing, and the on-site Coulomb repulsion is sufficiently high, one recovers the localization effect of  $U$ .

It is important to emphasize that for this result, the deduction of the exact, interacting, quantum mechanical many-body ground state at half filling, in a two-band system and two dimensions was needed [5]. In our knowledge, at the moment, the obtained state represents the unique explicitly given exact ground state of this type.

## II.2 Delocalization in quasi one-dimensional structures

In the search for similar effects in other type of structures one detected delocalization effects emerging in the presence of  $U$  in chain structures holding quadrilateral cells in the presence of external magnetic field perpendicular to the plane of the chain [6].

One of the most spectacular of these is related to a correlated half-metallic state. In this phase, the electrons holding  $\sigma$  spin projection are all localized on individual lattice sites, their movement being prohibited. In the same time, the electrons with  $-\sigma$  spin projection are delocalized and mobile. Their localization length is large at  $N = 4N_c$ , but in this concentration region the system remains localized in the thermodynamic limit. However, the localization length becomes infinitely large above the carrier concentration  $N > 4N_c$ , where  $N$  represents the number of electrons while  $N_c$  the number of cells (three lattice sites per cell are present into the system). The parameter space region where such a state emerges is

restricted, consequently can be tuned even by external parameters like external magnetic field, or site selective electric gate potentials [6], providing the potential possibilities for device design in various fields.

For other hopping parameters of the non-interacting part of the Hamiltonian one detected also other regions where delocalization processes occur. For example at  $n = N/(3N_c) \geq 5/3$  one has a region which has nonmagnetic and localized ground state at zero external magnetic field. By contrast, at finite external magnetic fields the ground state becomes a nonsaturated ferromagnet. This is a localized and insulating state at  $n = 5/3$ , but delocalized and itinerant at  $n > 5/3$  [6].

### References

- [1] Z. Gulácsi, Phys. Rev. **B69**, 054204 (2004).
- [2] N. Paris et. al. Phys. Rev. Lett. **98**, 046403 (2007).
- [3] S. S. Kancharla, E. Dagotto, Phys. Rev. Lett. **98**, 016402 (2007).
- [4] Z. Gulácsi, A. Kampf, D. Vollhardt, Phys. Rev. Lett. **99**, 026404 (2007).
- [5] Z. Gulácsi, Phys. Rev. **B77**, 245113 (2008).
- [6] Z. Gulácsi, A. Kampf, D. Vollhardt, Progr. Theor. Phys. Suppl. **176**, 1 (2008)

## ENTROPIC UNCERTAINTY RELATIONS

**Á. Nagy**

Department of Theoretical Physics, University of Debrecen,  
H–4010 Debrecen, Hungary

### Abstract

Entropic uncertainty relations are reviewed. Uncertainty relations involving Rényi entropy of order  $\alpha$  are presented. A link between Fisher and Rényi entropies is also emphasized.

### I. Introduction

The most well-known form of the uncertainty principle is the Heisenberg-Robertson uncertainty relation [1]. It gives a lower bound on the standard deviations for any pair of non-commuting observables:

$$V_{\hat{A}}(|\psi\rangle)V_{\hat{B}}(|\psi\rangle) \geq \frac{1}{4}|\langle\psi|[\hat{A}, \hat{B}]|\psi\rangle|^2, \quad (1)$$

which is the generalization of Heisenberg's inequality

$$V_{\hat{x}}(|\psi\rangle)V_{\hat{p}}(|\psi\rangle) \geq \frac{1}{4}, \quad [\hat{x}, \hat{p}] = i. \quad (2)$$

$$V_{\hat{A}}(|\psi\rangle) = \langle\psi|\hat{A}^2|\psi\rangle - \langle\psi|\hat{A}|\psi\rangle^2 \quad (3)$$

is the variance of  $\hat{A}$  in the state  $|\psi\rangle$  and the units are chosen so that  $\hbar = 1$ . In the 1980s it turned out, however, that the inequality (1) does not properly express the quantum uncertainty principle. The inequality (1) has been criticized on the grounds that the right-hand side of (1) is not a fixed

lower bound, but depends on the state  $|\psi\rangle$ . For example, when  $|\psi\rangle$  is an eigenstate of  $\hat{A}$ , then we obtain  $V_{\hat{A}}(|\psi\rangle) = 0$  and  $\langle\psi|[\hat{A}, \hat{B}]|\psi\rangle = 0$ , so there is no restriction on  $V_{\hat{B}}(|\psi\rangle)$  imposed by relation (1). Therefore entropic uncertainty relations were proposed instead. These give lower bounds to the sum of the Shannon information entropies. The first relations were obtained in [2] for the sum of position and momentum space Shannon entropies. Several entropic uncertainty relations were derived for finite-dimensional Hilbert spaces [3, 4, 5, 6, 7, 8, 9, 10, 11].

Bialynicki-Birula and Mycielski derived the uncertainty relation [2]:

$$S_{|\Psi|^2} + S_{|\Phi|^2} \geq 3(1 + \ln \pi). \quad (4)$$

$\Psi(\mathbf{r})$  is a wave function in the position space and  $\Phi(\mathbf{p})$  is its Fourier transform. The corresponding distribution functions are  $\varrho = |\Psi|^2$  and  $\gamma = |\Phi|^2$ . The position space and momentum space Shannon information entropies are defined as

$$S_{|\Psi|^2} = - \int \varrho(\mathbf{r}) \ln \varrho(\mathbf{r}) d\mathbf{r} \quad (5)$$

and

$$S_{|\Phi|^2} = - \int \gamma(\mathbf{p}) \ln \gamma(\mathbf{p}) d\mathbf{p}, \quad (6)$$

respectively.

## II. Rényi entropy

Rényi entropy is a one-parameter extension of Shannon entropy. Rényi entropy has already turned to be important in several fields of physics, e.g. in the analysis of quantum entanglement [12], quantum communication protocols [13], quantum correlations [14] or localization properties [15].

Rényi entropy of order  $\alpha$  for a  $D$  dimensional probability density function  $f(r_1, \dots, r_D)$  normalized to one is defined by

$$R_f^\alpha \equiv \frac{1}{1-\alpha} \ln \int f^\alpha(\mathbf{r}) d\mathbf{r}, \quad \text{for } 0 < \alpha < \infty, \quad \alpha \neq 1, \quad (7)$$

where  $\mathbf{r}$  stands for  $r_1, \dots, r_D$ . It is straightforward to show that the Rényi entropy tends to the Shannon entropy when  $\alpha \rightarrow 1$ .

Bialynicki-Birula derived an uncertainty relation [16] for the Rényi entropy sum:

$$R_{|\Psi|^2}^\alpha + R_{|\Phi|^2}^\beta \geq f(\alpha, \beta), \quad \frac{1}{\alpha} + \frac{1}{\beta} = 2, \quad (8)$$

$$f(\alpha, \beta) = \frac{3N}{2} \left[ \frac{1}{\alpha-1} \ln \left( \frac{\alpha}{\pi} \right) + \frac{1}{\beta-1} \ln \left( \frac{\beta}{\pi} \right) \right]. \quad (9)$$

This uncertainty relation reaches the Shannon entropic uncertainty relation (4) in the limit  $\alpha \rightarrow 1$ .

In order to derive further inequalities we defined the Rényi entropy power of index  $\alpha$  [17] by

$$\begin{aligned} N_f^\alpha &\equiv \left( \frac{\alpha}{2\alpha-1} \right)^{\frac{2\alpha-1}{\alpha-1}} \frac{1}{2\pi} \exp \left( \frac{2}{D} R_f^\alpha \right) \\ &= \beta^{1/(1-\beta)} \frac{1}{2\pi} \exp \left( \frac{2}{D} R_f^\alpha \right), \quad \alpha > 1/2. \end{aligned} \quad (10)$$

The Rényi entropy power is an extension of Shannon entropy power  $N_f$  and when  $\alpha \rightarrow 1$  then  $N_f^\alpha \rightarrow N_f = \frac{1}{2\pi e} e^{\frac{2}{D} S_f}$ . It has the property [18]

$$N_f^\alpha > N_f^{\alpha'}, \quad \alpha < \alpha'. \quad (11)$$

The Rényi and Shannon information powers satisfy the inequalities:

$$N_f^\alpha \geq N_f, \quad \frac{1}{2} < \alpha \leq 1 \quad (12)$$

and

$$N_f^\alpha \leq N_f, \quad \alpha \geq 1. \quad (13)$$

The Rényi uncertainty relation can be expressed in terms of Rényi entropy power in a compact form by

$$N_{|\Psi|^2}^\alpha N_{|\Phi|^2}^\beta \geq 1/4. \quad (14)$$

### III. Fisher-Rényi entropy product

Fisher information of the probability density function  $f$  [19] is given by

$$I_f \equiv \int \frac{|\nabla f(\mathbf{r})|^2}{f(\mathbf{r})} d\mathbf{r}. \quad (15)$$

Combining the so-called isoperimetric inequality  $I_f N_f \geq D$  [18] and inequality (12) we obtain the Rényi-Fisher relation

$$I_f N_f^\alpha \geq D \quad \text{with } \alpha \in (1/2, 1]. \quad (16)$$

This inequality can be extended to different parameters:

$$I_f N_f^\alpha > I_f N_f^{\alpha'} \geq D \quad \text{with } 1/2 < \alpha < \alpha' \leq 1, \quad (17)$$

applying the inequality (11).

Making use of the Stam uncertainty relation  $I_{|\Psi|^2} \leq 4\sigma_{|\Phi|^2}^2$  where  $\sigma_{|\Phi|^2}^2$  is the variance of the distribution in momentum space  $|\Phi|^2$  we obtain a Stam type uncertainty relation for Rényi entropy power

$$N_{|\Psi|^2}^\alpha \geq \frac{D}{4\sigma_{|\Phi|^2}^2}, \quad \alpha \in (1/2, 1]. \quad (18)$$

The same procedure in momentum space leads to the inequality:

$$N_{|\Phi|^2}^\alpha \geq \frac{D}{4\sigma_{|\Psi|^2}^2}, \quad \alpha \in (1/2, 1] \quad (19)$$

where  $\sigma_{|\Psi|^2}^2$  is the variance of the distribution  $|\Psi|^2$  in position space.

Inequalities (18) and (19) can straightforwardly be extended to different parameters:

$$N_{|\Psi|^2}^\alpha > N_{|\Psi|^2}^{\alpha'} \geq \frac{D}{4\sigma_{|\Phi|^2}^2}, \quad 1/2 < \alpha < \alpha' \leq 1 \quad (20)$$

and

$$N_{|\Phi|^2}^\alpha > N_{|\Phi|^2}^{\alpha'} \geq \frac{D}{4\sigma_{|\Psi|^2}^2}, \quad 1/2 < \alpha < \alpha' \leq 1. \quad (21)$$

We have recently extended the inequalities presented above to single particle densities of  $N$ -particle systems. The single particle densities in position and momentum spaces are given by

$$\rho(\mathbf{r}) = \int |\Psi(\mathbf{r}_1, \mathbf{r}_2, \dots, \mathbf{r}_N)|^2 d\mathbf{r}_2 \dots d\mathbf{r}_N \quad (22)$$

and

$$\gamma(\mathbf{p}) = \int |\Phi(\mathbf{p}_1, \mathbf{p}_2, \dots, \mathbf{p}_N)|^2 d\mathbf{p}_2 \dots d\mathbf{p}_N, \quad (23)$$

respectively. The density is normalized to one.

The relations (16)-(21) can readily be transcribed in terms of the corresponding one-particle probability densities  $\rho(\mathbf{r})$  and  $\gamma(\mathbf{p})$  by

$$I_\rho N_\rho^\alpha \geq D, \quad I_\gamma N_\gamma^\alpha \geq D \quad \text{with } \alpha \in (1/2, 1]. \quad (24)$$

and for different parameters:

$$I_\rho N_\rho^\alpha > I_\rho N_\rho^{\alpha'} \geq D \quad \text{with } 1/2 < \alpha < \alpha' \leq 1 \quad (25)$$

and

$$I_\gamma N_\gamma^\alpha > I_\gamma N_\gamma^{\alpha'} \geq D \quad \text{with } 1/2 < \alpha < \alpha' \leq 1. \quad (26)$$

The superadditivity and subadditivity of the Fisher and Shannon informations, respectively, have been used to prove the validity of Stam's uncertainty [20, 21] relation and Shannon uncertainty [22, 21] relation for single-particle densities in position and momentum spaces. Using the one-particle densities in position and momentum space, the inequalities take the form:

$$I_\rho \leq 4\sigma_\gamma^2, \quad I_\gamma \leq 4\sigma_\rho^2 \quad (27)$$

and

$$N_\rho N_\gamma \geq 1/4. \quad (28)$$

Note, that the relationship between the single particle and N-particle variance is  $\sigma_{|\Psi|^2}^2 = N\sigma_\rho^2$  in coordinate space and there is a similar expression for momentum space. Now, using the uncertainty relations and the inequalities (18),(19) and (12) it is fulfilled that

$$N_\rho^\alpha \geq \frac{D}{4\sigma_\gamma^2}, \quad N_\gamma^\alpha \geq \frac{D}{4\sigma_\rho^2}, \quad \alpha \in (1/2, 1] \quad (29)$$

and

$$N_\rho^\alpha N_\gamma^\alpha \geq 1/4, \quad \alpha \in (1/2, 1]. \quad (30)$$

For  $\alpha = 1$  we recover the Shannon uncertainty relation which is sharp, and which saturates for Gaussian functions.

In summary, it is emphasized that uncertainty relations can be derived for single particle densities of many particle systems. Inequalities involving Rényi entropy of order  $\alpha$  are presented. A link between Fisher and Rényi entropies is also emphasized.

This work was supported by the grant OTKA No. K 67923.

## References

- [1] H. P. Robertson, Phys. Rev. **34**, 163 (1929).
- [2] I. Bialynicki-Birula and I. Mycielski, Commun. Math. Phys. **44**, 129 (1975).
- [3] D. Deutsch, Phys. Rev. Lett. **50**, 631 (1983).
- [4] M. H. Partovi, Phys. Rev. Lett. **50**, 1883 (1983).
- [5] J. B. M. Uffink and J. Hilgevoord, Found. Phys. **15**, 925 (1985).
- [6] K. Kraus, Phys. Rev. D **35**, 3070 (1987).
- [7] H. Massen and J. B. M. Uffink, Phys. Rev. Lett. **60**, 1103 (1988).
- [8] J. Sánchez, Phys. Lett. A **173**, 233 (1993).

- [9] M. J. W. Hall, Phys. Rev. Lett. **74**, 3307 (1995).
- [10] J. Sánchez-Ruiz, Phys. Lett. A **244**, 189 (1998).
- [11] J. I. de Vicente and J. Sánchez-Ruiz, Phys. Rev. A **77**, 042110 (2008).
- [12] O. Gühne and M. Lewenstein, Phys. Rev. A **70**, 022316 (2004); G. Adesso, A. Serafini and F. Illuminati, Phys. Rev. A **70**, 022318 (2004); A. Bovino, G. Castagnolli, A. Ekert, P. Horodecki, C. M. Alves and A. V. Serfienko, Phys. Rev. Lett. **95**, 240407 (2005).
- [13] R. Renner, N. Gisin and B. Kraus, Phys. Rev. A **72**, 012332 (2005); V. Giovannetti and S. Lloyd, Phys. Rev. A **69**, 062307 (2004).
- [14] P. Lévay, S. Nagy and J. Pipek Phys. Rev. A **72**, 022302 (2005).
- [15] D. G. Arbo, C. O. Reinhold, J. Burgdörfer, A. K. Pattanayak, C. L. Stokely, W. Zhao, J. C. Lancaster and F. B. Dunning, Phys. Rev. A **67**, 063401 (2003).
- [16] I. Bialynicki-Birula, Phys. Rev. A **74**, 052101 (2006).
- [17] E. Romera and Á. Nagy, Phys. Lett. A **372**, 6823 (2008).
- [18] A. Dembo, T. M. Cover, and J. A. Thomas, IEEE Trans. Inf. Theory **37**, 1501 (1991).
- [19] R. A. Fisher, Proc. Cambridge Philos. Soc. **22**, 700 (1925).
- [20] M. Hoffmann Ostenhof and T. Hoffmann Ostenhof, Phys. Rev. A **16**, 1782 (1977).
- [21] E. A. Carlen, J. Funct. Anal. **101**, 194 (1991).
- [22] S. R. Gadre, S. B. Sears, S. J. Chakravorty and R. D. Bendale, Phys. Rev. A **32**, 2602 (1985).

**TOPOLOGICAL PHASE TRANSITION AS A CROSSOVER****S. Nagy<sup>1</sup>, I Nándori<sup>2</sup>, K. Sailer<sup>1</sup>**<sup>1</sup> Department of Theoretical Physics, University of Debrecen, Debrecen, Hungary<sup>2</sup> Institute of Nuclear Research of the Hungarian Academy of Sciences, H-4001  
Debrecen, P.O.Box 51, Hungary**Abstract**

The renormalization group flow is presented for the two-dimensional sine-Gordon model within the framework of the functional renormalization group method by including the wavefunction renormalization. We give a more general view on the topological phase transition appearing in the model by showing that it is a simple crossover between two competing attractive regions on the phase diagram.

**I. Introduction**

Phase transitions are known in our everyday life, for example the melting of ice, where a small change of a macroscopic observable (e.g. the temperature) is accompanied by a sudden change in the measurable macroscopic properties. Similar phase transitions in quantum systems at zero temperature can occur due to a small change of some microscopic parameter, e.g. in the normal to superfluid transition in  $He$  films which infinite order or topological phase transition can be modelled by the two-dimensional sine-Gordon model. The conventional phase transition is accompanied by a formation of a long range order in the ordered phase. In two dimensions according to the so-called Mermin-Wagner-Coleman theorem the quantum fluctuations destroy the spatial order, however only topological order is allowed. The topological phase transition in the sine-Gordon model is

a Kosterlitz-Thouless-Berezinski (KTB) type phase transition which was mapped so far in the vicinity of the transition point. It implies that the evolution of the macroscopic parameters takes into account a small amount of quantum fluctuations which corresponds to the ultra-violet (UV) approximation. The proper treatment of the model needs considering all the quantum fluctuation from UV to infrared (IR) scalings.

It is only the functional renormalization group (RG) method which is capable of taking into account the fluctuations systematically. The Wegner-Houghton RG method orders the fluctuations according to their frequency, the functional Callan-Symanzik scheme orders them by their amplitude, or the RG method based on the average effective action averages out the field variable with respect to an increasing volume which correspond to a decreasing momentum scale. Since the systematical consideration is the root of all type of RG methods, it is not so surprising that there is a general equation which can describe all the types of RG treatments mentioned above [1]. The renormalization is usually used to remove divergences of loop integrals, and is performed perturbatively according to loop- or some small parameter (usually small coupling) expansion. Perturbative treatments are efficient when the energy scale of the theory where it is defined is not so far from the observational scale. When these scales are well separated then the functional renormalization group (RG) method seems a good candidate to treat the theories. The functional RG is the most flexibly usable non-perturbative method and is one of the most dynamically developing branch in modern physics. The method can provide us the results of the perturbative RG treatment, and furthermore it is suitable for (i) determining the low energy behaviour of the model (the IR values of the couplings), (ii) mapping out the phase structure according to IR scaling of the couplings and their sensitivity from the ultraviolet (UV) initial values, and (iii) giving conceptual predictions in field theory.

It is well-known that an infinitesimal change in the observational scale can cause changes in the couplings in the same order, because the RG flows are continuous. Then, how can cause a small change of a physical quantity sudden changes in the phases? The question can be answered by the RG method. During the RG flow one integrates out the fluctuations systematically one after the other. Although each fluctuation contributes

an infinitesimal change for the value of the couplings but the evolution covers the whole scale starting from the UV into the deep IR one and takes into account infinitely many quantum fluctuations. These infinite number of contributions accumulate and can result in non-continuous flow for the couplings which microscopic (or UV) value differs infinitesimally due to a small change of a certain physical quantity. This reasoning clearly shows why the known treatment of the topological phase transition in the vicinity of the transition point is incomplete and why the problem needs a proper RG investigation.

## II. The model

The two-dimensional (2D) sine-Gordon (SG) model, defined by the bare action

$$S = \int_x \left[ \frac{1}{2} (\partial_\mu \varphi)^2 + u \cos(\beta \varphi) \right] \quad (1)$$

in Euclidean spacetime, has already received a considerable amount of attention since it is the simplest non-trivial quantum field theory with compact variables. This feature is common with non-Abelian gauge theories and is supposed to be the key to their confinement mechanism. In two dimension this is the driving force to form a nontrivial phase structure. The SG model is known to belong to the universality class of the 2D Coulomb gas and the 2D-XY spin model which have received important applications in condensed matter systems, e.g. describing the KTB phase transition of vortices in a thin superfluid film. There is a continuous interest in the literature in constructing SG type models to understand better the vortex dynamics of condensed matter systems [2].

The functional renormalization group equation for the effective action of an Euclidean field theory is [4]

$$k \partial_k \Gamma_k = \frac{1}{2} \text{Tr} \frac{k \partial_k R_k}{R_k + \Gamma''_k} \quad (2)$$

where the notation  $' = \partial/\partial\varphi$  is used and the trace Tr stands for the integration over all momenta. We use a power-law type regulator function

$R_k = p^2(k^2)(p^2)^b$  with the parameter  $b \geq 1$ . Eq. (2) has been solved over the functional subspace defined by the ansatz

$$\Gamma_k = \int_x \left[ \frac{z}{2} (\partial_\mu \varphi_x)^2 + V_k(\varphi_x) \right], \quad (3)$$

with the local potential  $V_k(\varphi) = \sum_{n=1}^{\infty} u_n(k) \cos(n\varphi)$  and the field-independent wave-function renormalization  $z(k)$ . Eq. (2) leads to the evolution equations

$$(2 + k\partial_k)\tilde{u}_1 = \frac{1}{4\pi z}\tilde{u}_1, \quad (4)$$

$$k\partial_k z = -\frac{\tilde{u}_1^2}{z^{2-2/b}} c_b, \quad (5)$$

where the dimensionless couplings  $\tilde{u}_n = k^{-2}u_n$  are introduced, and

$$c_b = \frac{b}{48\pi} \Gamma\left(3 - \frac{2}{b}\right) \Gamma\left(1 + \frac{1}{b}\right). \quad (6)$$

The Coleman fixed point separates the renormalizable, broken symmetric phase ( $1/z < 8\pi$ ) and the non-renormalizable, symmetric phase ( $1/z > 8\pi$ ) which can be also obtained using the local potential approximation (LPA) [3, 6]. Eqs. (4) and (5) provide similar evolution around the KTB fixed point as was already obtained by a perturbative RG analysis, the flow equation approach, and also by the real-space RG for the two-dimensional Coulomb gas. The KTB phase transition is characterized by the exponential dependence of the correlation length on the inverse of the square-root of the reduced temperature  $t \propto \tilde{u}_1^{*2}$ . The correlation length  $\xi$  can be read off from the scale  $k^* \sim 1/\xi$  where the RG trajectories show up their turning points and one obtains

$$\xi \sim e^{\sqrt{\pi}/(\tilde{u}_1^* 8\sqrt{c_b}) + \tilde{u}_1^*(b-1)(2b-1)\sqrt{c_b} 2^{1-6/b} \pi^{5/2-2/b} b^{-2} + \mathcal{O}(\tilde{u}_1^{*2})} \quad (7)$$

which is the typical scaling law for KTB type phase transitions, modified by analytic corrections vanishing for  $\tilde{u}_1^* \rightarrow 0$ . Using Eqs. (4) and (5) the critical exponent  $\eta$  can also be calculated via the vortex-vortex correlation function and it is proved to take the value  $\eta = 1/4$  independently of the parameter  $b$ .

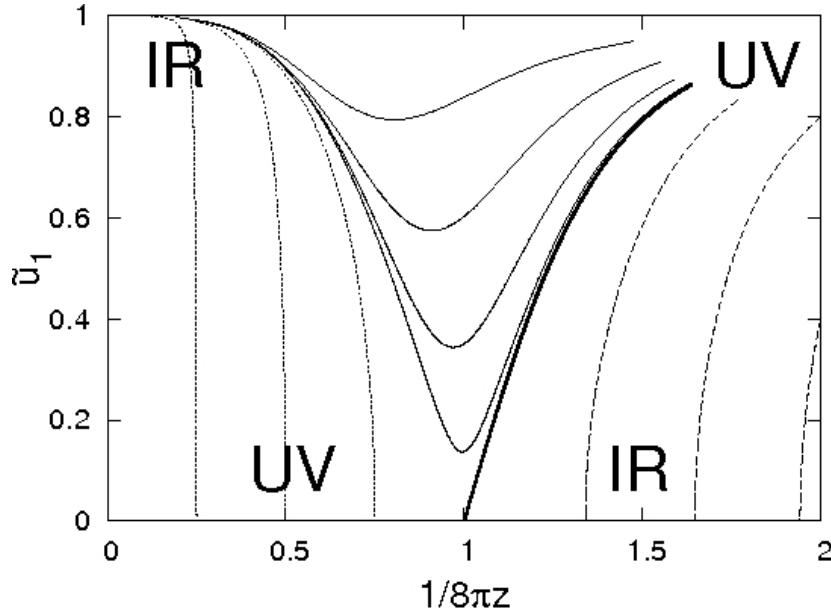


Figure 14: The phase structure of the SG model given by the numerical solution of Eqs. (8) and (9). The trajectories flow from right to left.

### III. IR scaling

By restricting the solution to the fundamental mode  $\tilde{u}_1$  one obtains the evolution equations

$$(2 + k\partial_k)\tilde{u}_1 = \frac{1}{2\pi\tilde{u}_1 z} \left[ 1 - \sqrt{1 - \tilde{u}_1^2} \right], \quad (8)$$

$$k\partial_k z = -\frac{1}{24\pi} \frac{\tilde{u}_1^2}{(1 - \tilde{u}_1^2)^{\frac{3}{2}}}, \quad (9)$$

and the corresponding RG trajectories can be seen in Fig. 14. They end in a line of Gaussian IR fixed point in the non-renormalizable phase, when  $1/z > 8\pi$ . There the evolution of the wave-function renormalization  $z$  is extremely weak, and is practically negligible, therefore LPA can be used and the well-known IR scaling is recovered. There is a line of Gaussian fixed points too, when  $1/z < 8\pi$ , but these fixed points are UV. The IR scaling is difficult to

establish numerically in this phase because of the instability of the Fourier expansion [1] in any RG scheme, used so far. It seems from Fig. 14 that  $z \rightarrow \infty$  as the scale  $k$  is decreased, while  $\tilde{u}_1$  remains finite. Fig. 14 nicely demonstrates that the hyperbolic nature of the flow in the vicinity of the KTB-Coleman point stems from global effects, the competition between two regions of the phase diagram. This is the attraction of the line of Gaussian IR fixed points of the symmetrical phase, dominated by the kinetic energy on the one hand and of the non-Gaussian, IR fixed point which is dominated by the potential energy on the other.

The effective potential built up in the IR region makes the evolution equation singular, which is typical for phases with spontaneously broken symmetry, automatically guaranteeing the superuniversality for the potentials. It implies that the treatment with no expansion should also give the superuniversal potential  $\tilde{V}_{k \rightarrow 0} = -\frac{1}{2}\phi^2$  due to the Maxwell cut and  $1/z(k \rightarrow 0) = 0$ .

## References

- [1] I. Nandori, S. Nagy, K. Sailer, A. Trombettoni, *Comparison of renormalization group schemes for sine-Gordon type models*, Phys. Rev. D**80** (2009) 025008.
- [2] I. Nandori, U. D. Jentschura, S. Nagy, K. Sailer, K. Vad, S. Mészáros, *On the applicability of the layered sine-Gordon model for Josephson-coupled high- $T_c$  layered superconductors*, J. Phys.: Condens. Matter 19 (2007) 236226; I. Nandori, U. D. Jentschura, S. Nagy, K. Sailer, K. Vad, S. Mészáros, *Applicability of layered sine-Gordon models to layered superconductors: II. The case of magnetic coupling* J. Phys.: Condens. Matter 19 (2007) 496211
- [3] S. Nagy, J. Polonyi, K. Sailer, *Effective Potential for the Massive Sine-Gordon Model*, J. Phys. A**39** (2006) 8105; S. Nagy, I. Nandori, J. Polonyi, K. Sailer, *Renormalizable parameters of the sine-Gordon model*, Phys. Lett. B**647** (2007) 152.

- [4] S. Nagy, I. Nandori, J. Polonyi, K. Sailer, *Generalized universality in the massive sine-Gordon model*, Phys. Rev. D**77** (2008) 025026.
- [5] S. Nagy, I. Nandori, J. Polonyi, K. Sailer, *Functional renormalization group approach to the sine-Gordon model*, Phys. Rev. Lett. **102** (2009) 241603.
- [6] V. Pangon, S. Nagy, J. Polonyi, K. Sailer, *Quantum censorship in two dimensions*, arXiv:0907.0496.

**INVESTIGATION OF HIGHER LYING EXCITED STATES  
OF PYRAZINE****G. J. Halász<sup>1</sup>, A. Papp<sup>2</sup>, C. Woywod<sup>3</sup>, Á. Vibók<sup>2</sup>**<sup>1</sup> Department of Information Technology, University of Debrecen, H-4010 Debrecen, PO Box 12, Hungary<sup>2</sup> Department of Theoretical Physics, University of Debrecen, H-4010 Debrecen, PO Box 5<sup>3</sup> Theoretical Chemistry (CTCC), Chemistry Department, University of Tromsø, N-9037 Tromsø**Abstract**

The electronic spectrum of pyrazine has been studied by employing the complete active space self-consistent field (CASSCF) and complete active space multiconfigurational second-order perturbation theory (CASPT2) methods. Oscillator strengths have been calculated for various electronic transitions. Basis sets and active spaces were selected to provide highly accurate results for vertical excitation energies and oscillator strengths. The aug-cc-pVDZ basis set extended by Rydberg functions has been used to calibrate the methodology by comparison with previously reported calculations and with experiment, in particular with the goal to optimize the active space. The best active space found by this procedure has then been combined with the aug-cc-pVTZ basis set including Rydberg functions to provide very accurate estimates for the properties of various singlet excited states of pyrazine. While many of the assignments made in previous studies could be confirmed, there are also several new aspects emerging from the present investigation.

## I. Introduction

The electronic spectrum of pyrazine has been the subject of several experimental [1, 2, 3, 4, 5] and theoretical [6, 7, 8, 9, 10] studies. This molecule has for a long time been of interest not only because it provides insight into the molecular dynamics of simple aromatic systems [11, 12, 13, 14, 15] but also because it is a fundamental parent system for numerous biologically active compounds such as nicotinic acid and the nucleotides cytosine, uracil, and thymine, etc. [16, 17, 18, 19, 20, 21] Innes and coworkers published a very important review article covering experimental and theoretical studies on the electronic states of azabenzenes up to 1988 [1]. Extensive theoretical work on this subject has been performed by Fülscher and Roos [6, 7]. They also used the complete active space self-consistent field (CASSCF) and complete active space multiconfigurational second-order perturbation theory (CASPT2) methods to investigate the dependence of computed valence excitation energies and transition moments on the basis sets. In 1997 Del Bene, Watts and Bartlett performed a series of equation of motion coupled-cluster (EOM-CC) calculations and compared the obtained results to available experimental and theoretical data [8]. Not only for the singlet but also for the triplet states of this molecule several *ab initio* and density functional calculations were reported by Weber and Reimers [9]. Recently theoretical results for the vertical excitation energies of pyrazine have been presented by Li, Wan and Xu [10]. They have studied the ground and excited states of this molecule and compared their results to available theoretical and experimental data. There are many inconsistencies among the results obtained in these studies. For example the ordering of the vertical excitation energies of the different states has been quite controversial, this strongly depends on the electronic structure methods and basis sets. But there is agreement that the ground and low-lying first and second excited states have the following electronic features:  $S_0(^1A_g)$ ,  $[S_1(^1B_{3u}); n\pi^*]$  and  $[S_2(^1B_{2u}); \pi\pi^*]$ .

By using the CASSCF and CASPT2 methods, one of the goals of the present work has been to find a suitable basis set and active space not only for the description of valence excited states but also of Rydberg states. We started by trying to reproduce the experimental data and the numerical results obtained by Fülscher and Roos [7] by employing the aug-cc-pVDZ

basis set, adding Rydberg functions to the center of the molecule, and by varying the active spaces. After calibrating the electronic strucutre model we then applied the most efficient active space in combination with a larger basis set, again including Rydberg functions, to perform new calculations in order to obtain more accurate values than previously available, in particular for the higher lying states.

One perspective of the present work is to use the experience obtained on this system to later extend our studies in order to calculate very accurately potential energy surfaces for those states, localizing conical intersections between different electronic states and eventually to performe dynamical calculations.

This paper is organized as follows: the computational details of the calculations are explained in Sec. II. In Sec. III, the results are presented and discussed. The summary and conclusions are given in Sec. IV.

## II. Methods and numerical details

The calculations were carried out partly at the Jülich Supercomputing Centre on an IBM p6 575 Cluster JUMP and partly at the Leibniz Rechenzentrum of the Bavarian Academy of Sciences on a Linux Cluster. The standard CASSCF and CASPT2 calculations were performed with the MOLPRO program package [19]. The geometries of the ground state ( $S_0(^1A_g)$ ) of pyrazine were optimized at the CASPT2 level employing Dunning's augmented correlation consistent aug-cc-pVDZ and aug-cc-pVTZ basis sets [20, 21].

For a better description of relatively diffuse  $\pi^*$  excited valence states and in particular of Rydberg states, a set of molecule centered diffuse s,p and d functions has been added to both the aug-cc-pVDZ and aug-cc-pVTZ basis sets [22].

The quality of the results strongly depends on the size of the active space employed. The active space configurations are obtained by forming all spin-allowed excitations involving n electrons distributed over m orbitals. An active space can be denoted as (n,m). We have constructed several different active spaces and all of them are summarized in Table 1. The

smallest one is given by the combination (10,8) and the largest one by the label (12,15). CASSCF calculations were performed for the evaluation of excitation energies using all the different active spaces. By comparing the accuracy of the results and the computational times for the different CASSCF versions we arrived at the (12,14) combination as the best solution for our purposes.

One criterion for the precision of the different active space combinations can be derived from the observation that the CASSCF method frequently tends to overestimate vertical excitation energies since only a very small part of the dynamic electron correlation energy is taken into account by this approach. The quality of an active space is therefore connected to the property of predicting low vertical excitation energies for the electronic states of interest.

In this study, we are concentrating exclusively on singlet states. In order to achieve maximum accuracy, the ground states in each irreducible representation have been optimized individually in the CASSCF calculations. The first excited states in the  $A_g$ ,  $B_{1u}$ ,  $B_{2u}$  and  $B_{3u}$  symmetries have been computed by converging an averaged CASSCF functional with weights of 0.05 and 0.95 for the first and second root, respectively. The case of the CASSCF calculation with aug-cc-pVTZ basis set for the  $2B_{2u}$  state represents an exception because the ratio had to be adjusted to 0.03 and 0.97 in order to reach convergence. No excited states have been calculated in the  $B_{1g}$ ,  $B_{2g}$ ,  $B_{3g}$  and  $A_u$  symmetries.

The bulk of dynamic electron correlation energy is considered by performing CASPT2 calculations based on the CASSCF reference wave functions. More precisely, the “rs2c” version of the CASPT2 module as implemented in the MOLPRO package has been employed [19]. In order to deal with intruder state problems, a level shift of 1.5 was used throughout in the CASPT2 calculations.

### III. Results and discussion

The vertical excitation energies and oscillator strengths are calculated at the geometry of the global minimum. The lowest excited singlet state is

of  $n\pi^*$  character. The most important contribution to this electronic state is the ( $6a_g \rightarrow 2b_{3u}$ ) excitation (Fig. 1). The second excited singlet state at the ground state equilibrium geometry is of  $\pi\pi^*$  character and the two most important configurations in the CI expansion for this state are the ( $1b_{1g} \rightarrow 2b_{3u}$ ) and ( $1b_{2g} \rightarrow 1a_u$ ) excitations (Fig. 2).

The CASSCF and CASPT2 energies, vertical excitation energies and oscillator strengths obtained with the extended aug-cc-pVDZ and aug-cc-pVTZ basis sets and (12,14) active space are presented in Tables 2 and 3. The CASPT2 oscillator strengths are calculated by combining the transition dipole moment values obtained at the CASSCF level of theory with the vertical excitation energies predicted by the CASPT2 method.

In Table 2 we also include the results of Fülscher and Roos [7]. The results compiled in Table 7 of Ref. [7] are reported here because the size of the basis set applied in Ref. [7] is similar to the aug-cc-pVDZ bases utilized for the present calculations. The agreement between the CASSCF and CASPT2 results is generally satisfactory. The most significant deviation can be found for the  $2B_{2u}$  state. In particular the disagreement on the oscillator strength of this state is striking.

While the CASPT2 predictions for the vertical excitation energy of the  $2B_{2u}$  state appear to be consistent, there is also a substantial difference between the CASSCF excitation energies for this state obtained in Ref. [7] and in the present study. This problem becomes even more interesting if one considers that according to our calculations the  $2B_{2u}$  state is one of the rare cases for which the CASSCF method is yielding a lower vertical excitation energy than the CASPT2 approach, a result that is confirmed by application of the extended aug-cc-pVTZ basis (Table 3).

Can we turn to experimental data to find the true values of  $f$  and  $\Delta E$  for the  $2B_{2u}$  state? Ref. [1] alleges that  $2B_{2u}$  is a 3p Rydberg excitation with a  $T_{00} \sim 6.84$  eV and  $f \sim 0.25$ . However, Ref. [1] also maintains that the symmetry assignment is questionable and that the band could also correspond to  $B_{1u}$  symmetry. Ref. [4] does not clearly identify the  $2B_{2u}$  state at all but refers in analogy to benzene to a  $E_{1u}$ -like  $\pi\pi^*$  excited state with a vertical excitation energy  $\Delta E = 7.67$  eV and  $f = 0.72$ , which is probably the  $2B_{1u}$  state.

Therefore we unfortunately do not have clear experimental evidence for  $T_{00}$ ,  $\Delta E$  and  $f$  of the  $2B_{2u}$  state, but the present calculations clearly support the assignment by Ref. [1] that this state is of Rydberg character. This fact may yield an explanation for the large disagreement between the oscillator strength predictions made for the  $2B_{2u}$  state by Ref. [7] and by our results. The basis set employed for the calculations described in Ref. [7] does not include any Rydberg type functions and is consequently not appropriate for representing the diffuse  $2B_{2u}$  state of pyrazine.

Inspection of Table 3 reveals that our presumably most accurate estimates for the  $2B_{1u}$  and  $2B_{2u}$  states place them close in energy but assign very different oscillator strengths to them. If this is correct, then the  $2B_{2u}$  spectrum would be almost completely obscured by the  $2B_{1u}$  absorption band. The doubts about the assignment of the  $2B_{2u}$  band expressed in Ref. [1] may have been well justified.

A further analysis of the CASPT2 data compiled in Table 3 for  $\Delta E$  and  $f$  indicates a generally high accuracy for both valence and Rydberg states. Experimental estimates of vertical excitation energies are in many cases afflicted with a rather large uncertainty and it is therefore instructive to note that the theoretical  $\Delta E$  predictions are properly placed above all the available experimental  $T_{00}$  values, which are typically of much higher precision.

No experimental value for  $\Delta E$  of the  $2B_{3u}$  Rydberg state could be found, but we note a very large difference of nearly 3 eV between the CASPT2 prediction for the vertical excitation energy and the experimental  $T_{00}$  for this state given in Ref. [1]. However, the assignment is also questioned in Ref. [1] and  $T_{00}$  for this state may have to be placed significantly higher, which would improve the consistency with our calculation.

Calculated and measured oscillator strengths are consistent for the  $1B_{3u}$  and  $1B_{2u}$  states. In the case of  $f$  for the  $2B_{1u}$  state there is large disagreement between Refs. [1] and [4]. Our results match quite well with Ref. [1].

The sources Refs. [1] and [4] are unfortunately also not compatible regarding  $f$  for the  $1B_{1u}$  state. Our data are again closer to Ref. [1], although the agreement is not as good as for the  $2B_{1u}$  state.

## IV. Conclusions

In this study we have investigated the electronic spectrum of pyrazine by carrying out CASSCF and CASPT2 calculations. The vertical excitation energies have been calculated employing the aug-cc-pVDZ and aug-cc-pVTZ basis sets extended by a set of molecule-centered diffuse Rydberg functions. Estimates of vertical excitation energies have been obtained with an accuracy of 0.1-0.4 eV. The identification of the different states and the ordering of the vertical excitation energies has been discussed quite controversially by spectroscopists and theoreticians. From the theory point of view, this depends to some extent on the electronic structure methods and basis sets used for the calculations. Our results support most of the assignments made in Refs. [1, 4].

However, a few notable disagreements are also obtained. The placement of  $T_{00}$  of the  $2B_{3u}$  band at 6.75 eV made in Ref. [1] is not supported by our calculations. The oscillator strength predicted in Table 3 for the  $1B_{1u}$  valence state is significantly smaller than the values given by Refs. [1, 4]. This is also true for the  $2B_{2u}$  Rydberg state, which is probably much less intense than proposed in Ref. [1] and will be concealed by the  $2B_{2u}$  absorption band.

The experience obtained by working on this system will be used to continue studies on the excited states of pyrazine. We are planning to calculate very accurately potential energy surfaces for different electronic states including Rydberg states with the goal to localize conical intersections that may relevant for nonadiabatic effects on the spectroscopy of this system.

## ACKNOWLEDGMENTS

Å.V. acknowledges the computational resources provided by the John-von-Neumann Institute, Research Centre Jülich (Project ID `ehu01`). Thanks go also to the Leibniz Supercomputing Centre in Munich for providing computational resources on the Linux Cluster. C.W. would like to thank the Centre for Theoretical and Computational Chemistry at the University of Tromsø for continued support.

## References

- [1] K. K. Innes, I. G. Ross, and W. R. Moomaw, *J. Mol. Spectroscop.* **132**, 492 (1988).
- [2] I. Yamazaki, T. Murao, T. Yamanaka, and K. Yoshihara, *Faraday Discussions Chem. Soc.* **75**, 395 (1983).
- [3] J. Kommandeur, W. A. Majewski, W. L. Meerts, and D. W. Pratt, *Ann. Rev. Phys. Chem.* **38**, 433 (1987).
- [4] A. Bolovinos, P. Tsekeris, J. Philips, E. Pantos, and G. Anditsopoulou, *J. Mol. Spectrosc.* **103**, 240 (1984).
- [5] M. H. Palmer and I. C. Palmer, *Chem. Phys.* **157**, 187 (1991).
- [6] M. P. Fülscher, K. Andersson, and B. O. Roos, *J. Phys. Chem.* **96**, 9204 (1992).
- [7] M. P. Fülscher and B. O. Roos, *Theor. Chim. Acta* **87**, 403 (1994).
- [8] J. E. DelBene, J. D. Watts, and R. J. J. Bartlett, *J. Chem. Phys.* **106**, 6051 (1997).
- [9] P. Weber and J. R. Reimers, *J. Phys. Chem. A* **98** **21**, 103 (103).
- [10] Y. Li, J. Wan, and X. J. Xu, *J. Comp. Chem.* **28**, 1658 (2007).
- [11] G. A. Worth, H.-D. Meyer, and L. S. Cederbaum, *J. Chem. Phys.* **105**, 4412 (1996).
- [12] A. Raab, G. A. Worth, H.-D. Meyer, and L. S. Cederbaum, *J. Chem. Phys.* **110**, 936 (1999).
- [13] P. Puzari, R. S. Swathi, B. Sarkar, and S. J. Adhikari, *J. Chem. Phys.* **123**, 134317 (2005).
- [14] P. Puzari, B. Sarkar, and S. J. Adhikari, *J. Chem. Phys.* **125**, 194316 (2005).

- [15] W. Domcke, D. R. Yarkony, and H. Köppel, *Conical Intersections: Electronic Structure, Dynamics and Spectroscopy*, World Scientific, Singapore, 2004.
- [16] G. Stock, C. Woywod, W. Domcke, T. Swinney, and B. S. Hudson, *J. Chem. Phys.* **103**, 6851 (1995).
- [17] A. L. Sobolewski and W. Domcke, *Chem. Phys. Lett.* **180**, 381 (1991).
- [18] H. RongXing, Z. ChaoYuan, C. Chih-Hao, and L. Sheng-Hsien, *Sci. China Ser. B Chem.* **51**, 1166 (2008).
- [19] H.-J. Werner et al., Molpro, version 2006.1, a package of ab initio programs, 2006.
- [20] R. A. Kendall, T. H. Dunning, Jr., and R. J. Harrison, *J. Chem. Phys.* **96**, 6796 (1992).
- [21] T. H. Dunning, Jr., *J. Chem. Phys.* **90**, 1007 (1989).
- [22] The basis set coefficients are given in MOLPRO format as follows ('X' denotes the dummy center):  
's,X,.024624, .011253, .005858, .003346, .002048, .001324, .000893,  
.000624;  
C,1.8, 0.199154, 1.034881, -0.594226, 0.911796, -1.097305, 0.937498, -  
0.500904, 0.123768;  
p,X,.042335, .019254, .009988, .005689, .003476, .002242, .001511,  
.001055;  
C,1.8, 0.037112, -0.581451, -0.257041, -0.418473, 0.365405, -0.333179,  
0.192955, -0.052021;  
d,X,.060540, .027446, .014204, .008077, .004927, .003175, .002137,  
.001491;  
C,1.8, 0.039941, 0.231180, 0.358234, 0.384671, 0.076901, 0.068788, -  
0.030823, 0.008989;:
- [23] C. Woywod, W. Domcke, A. L. Sobolewski, and H.-J. Werner, *J. Chem. Phys.* **100**, 1400 (1994).

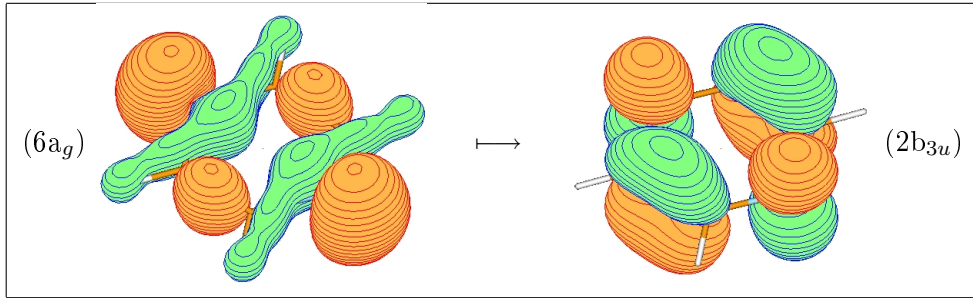


Figure 1: The most important contribution ( $\sim 82\%$ ) for the lowest excited singlet [ $S_1(^1B_{3u}); n\Pi^*$ ] electronic state.

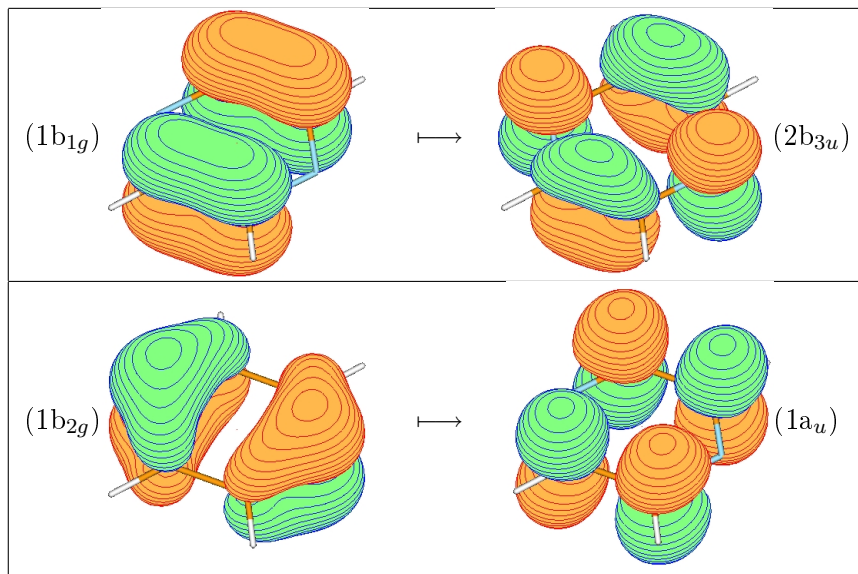


Figure 2: The two most important contributions ( $\sim 63\%$  and  $\sim 17\%$ ) for the second excited singlet [ $S_2(^1B_{2u}); \Pi\Pi^*$ ] electronic state.

Table 1: The following orbital spaces have been used in CASSCF calculations with the aug-cc-pVDZ basis sets extended by Rydberg functions in order to select the most appropriate active space. n is the number of active electrons and m is the number of orbitals over which they are distributed. The as6 (12,14) has been selected for the more accurate calculations summarized in Table 3.

doubly occupied								
as#(n,m)	a <sub>g</sub>	b <sub>3u</sub>	b <sub>2u</sub>	b <sub>1g</sub>	b <sub>1u</sub>	b <sub>2g</sub>	b <sub>3g</sub>	a <sub>u</sub>
as1 (10,8)	5	0	4	0	4	0	3	0
as2 (12,14)	5	0	4	0	4	0	2	0
as3 (10,15)	5	0	4	0	4	0	3	0
as4 (10,14)	5	0	4	0	4	0	3	0
as5 (10,15)	5	0	4	0	4	0	3	0
as6 (12,14)	5	0	4	0	4	0	2	0
as7 (10,12)	5	0	4	0	4	0	3	0
as8 (12,15)	5	0	4	0	4	0	2	0
as9 (12,14)	5	0	4	0	4	0	2	0
as10 (12,13)	5	0	4	0	4	0	2	0
as11 (10,13)	5	0	4	0	4	0	3	0

active space								
as#(n,m)	a <sub>g</sub>	b <sub>3u</sub>	b <sub>2u</sub>	b <sub>1g</sub>	b <sub>1u</sub>	b <sub>2g</sub>	b <sub>3g</sub>	a <sub>u</sub>
as1 (10,8)	1	2	0	1	1	2	0	1
as2 (12,14)	2	2	1	2	2	2	2	1
as3 (10,15)	2	3	2	3	2	2	0	1
as4 (10,14)	2	3	1	2	2	2	0	2
as5 (10,15)	2	3	1	3	2	2	0	2
as6 (12,14)	2	3	1	2	2	2	1	1
as7 (10,12)	1	3	1	2	2	2	0	1
as8 (12,15)	2	3	1	2	2	2	2	1
as9 (12,14)	1	3	1	2	2	2	2	1
as10 (12,13)	2	2	1	2	2	2	1	1
as11 (10,13)	2	2	1	2	2	2	1	1

Table 2: Total energies (E), given in a.u., vertical excitation energies ( $\Delta E$ ), given in eV, and oscillator strengths (f) of pyrazine. Columns labeled by (a) contain the results calculated with an aug-cc-pVDZ basis sets extended by Rydberg functions while the data in columns designated by (b) are taken from Table 7 in Ref. [7], calculated with a (4s3p2d/3s2p) ANO basis set.

	E(CASSCF)	$\Delta E$		f	
		a	a	b	a
1A <sub>g</sub> (V)	-262.867732				
2A <sub>g</sub> (R)	-262.586624	7.649	8.40		
1B <sub>3u</sub> (V)	-262.683880	5.003	5.19	0.013	0.014
2B <sub>3u</sub> (R)	-262.591904	7.506		0.010	
1B <sub>2u</sub> (V)	-262.680994	5.081	5.10	0.080	0.073
2B <sub>2u</sub> (R)	-262.604022	7.176	9.55	0.016	0.817
1B <sub>1g</sub> (-)	-262.599882	7.289			
1B <sub>1u</sub> (V)	-262.576766	7.918	8.51	0.024	0.103
2B <sub>1u</sub> (R)	-262.525957	9.300	9.65	0.918	0.966
1B <sub>2g</sub> (V)	-262.642307	6.134			
1B <sub>3g</sub> (-)	-262.559840	8.379	8.53		
1A <sub>u</sub> (-)	-262.648536	5.965	6.29		
	E(CASPT2)	$\Delta E$		f	
		a	a	b	b
1A <sub>g</sub> (V)	-263.501226				
2A <sub>g</sub> (R)	-263.189092	8.494	8.22		
1B <sub>3u</sub> (V)	-263.359506	3.856	3.85	0.010	0.010
2B <sub>3u</sub> (R)	-263.215713	7.769		0.010	
1B <sub>2u</sub> (V)	-263.326217	4.762	4.76	0.075	0.068
2B <sub>2u</sub> (R)	-263.216380	7.751	7.74	0.017	0.662
1B <sub>1g</sub> (-)	-263.258643	6.601			
1B <sub>1u</sub> (V)	-263.247221	6.912	6.69	0.021	0.081
2B <sub>1u</sub> (R)	-263.204237	8.081	7.53	0.798	0.754
1B <sub>2g</sub> (V)	-263.293201	5.661			
1B <sub>3g</sub> (-)	-263.198926	8.226	8.31		

Table 3: Results of CASSCF and CASPT2 calculations for pyrazine with the extended aug-cc-pVTZ basis set are compiled. Total energies (E) are given in a.u. and vertical excitation energies ( $\Delta E$ ) in eV. In addition, oscillator strengths (f) are reported. The experimental 0-0 transition energies  $T_{00}$  are taken from Refs. [1, 4], estimates of vertical excitation energies ( $\Delta E$ ) based on experimental data are provided by Ref. [4]. Values for  $\Delta E$  of the  $1B_{3u}$  and  $1B_{2u}$  states have also been obtained by MRCI calculations [23].

	E(CASSCF)	$\Delta E$	f	E(CASPT2)	$\Delta E$	f
$1A_g(V)$	-262.926534			-263.717351		
$2A_g(R)$	-262.610560	8.598		-263.413397	8.271	
$1B_{3u}(V)$	-262.742677	5.003	0.012	-263.567319	4.083	0.010
$2B_{3u}(R)$	-262.541957	10.465	0.014	-263.367581	9.518	0.013
$1B_{2u}(V)$	-262.737612	5.141	0.086	-263.539700	4.834	0.081
$2B_{2u}(R)$	-262.649808	7.530	0.009	-263.426546	7.913	0.009
$1B_{1g}(-)$	-262.657931	7.309		-263.476937	6.542	
$1B_{1u}(V)$	-262.634831	7.938	0.028	-263.464052	6.893	0.024
$2B_{1u}(R)$	-262.581663	9.384	0.909	-263.425769	7.934	0.768
$1B_{2g}(V)$	-262.702933	6.084		-263.514187	5.528	
$1B_{3g}(-)$	-262.613778	8.511		-263.413249	8.275	
$1A_u(-)$	-262.704619	6.039		-263.537350	4.898	
	$\Delta E_{exp.}$ (Ref. [4])	$\Delta E_{theo.}$ (Ref. [23])	$T_{00\ exp.}$ (Ref. [4])	$T_{00\ exp.}$ (Ref. [1])	$f\ exp.$ (Ref. [4])	$f\ exp.$ (Ref. [1])
$1A_g(V)$						
$2A_g(R)$				6.30		
$1B_{3u}(V)$		4.22	3.83	3.83	0.006	0.006
$2B_{3u}(R)$				(6.75)		
$1B_{2u}(V)$	4.81	5.05	4.69	4.69-4.81	0.062	0.100/0.060
$2B_{2u}(R)$				6.84		(0.250)
$1B_{1g}(-)$						
$1B_{1u}(V)$	6.51		6.31	6.30	0.720	0.150/0.100
$2B_{1u}(R)$	7.67			7.05	0.100	1.000/0.700
$1B_{2g}(V)$	6.10			5.45		
$1B_{3g}(-)$						
$1A_u(-)$						